Ballistic electron microscopy and spectroscopy of metal and semiconductor nanostructures

W. Yi, A.J. Stollenwerk, V. Narayanamurti *

School of Engineering and Applied Sciences, Harvard University, Cambridge, MA 02138, United States

ARTICLE INFO

ABSTRACT

Ballistic electron emission microscopy (BEEM) and its spectroscopy utilize ballistic transport of hot carriers as a versatile tool to characterize nanometer-scale structural and electronic properties of metallic and semiconducting materials and their interfaces. In this review, recent progress in experimental and theoretical aspects of the BEEM technique are covered. Emphasis is drawn to the development of BEEM in several emerging fields, including spin-sensitive hot-carrier transport through ferromagnetic thin films and multilayers, hot-electron spectroscopy and imaging of organic thin films and molecules, and hot-electron induced electroluminescence in semiconductor heterostructures. A brief discussion on BEEM of cross-sectional semiconductor heterostructures and advanced insulator films is also included.

© 2009 Elsevier B.V. All rights reserved.

Contents

* Corresponding address: School of Engineering and Applied Sciences, Harvard University, 29 Oxford Street, Pierce Hall 217A, Cambridge, MA 02138, United States. Tel.: +1 617 495 5829; fax: +1 617 496 5264.
E-mail address: venky@seas.harvard.edu (V. Narayanamurti).

1. Introduction

Electron and hole transport is of great interest for the design of electronic devices. The continuing trend of device miniaturization requires a better understanding of the fundamental physics of this phenomenon on the nanometer scale. The invention of the scanning tunneling microscope (STM) by Binnig and Rohrer in 1981 has made it possible to perform both spectroscopy and imaging of surfaces on the atomic scale [1,2]. Ballistic electron emission microscopy (BEEM) is a three-terminal configuration of STM that allows the characterization of electron transport through materials and material interfaces on the nanometer scale [3,4]. In BEEM, hot electrons with extra kinetic energies up to several electron volts (eV) are injected from a STM tip (emitter) across a vacuum tunneling gap into a thin metal (base) layer that forms a Schottky contact on a semiconductor (collector) substrate (see Fig. 1). Those electrons with the appropriate energy and momentum distribution can traverse the base ballistically over the Schottky barrier into the collector.

First introduced in 1988, BEEM was initially used to study properties of various metal–semiconductor (m–s) systems such as Schottky barriers, interface band structure, hot-electron attenuation lengths and scattering properties of overlying metal films [3,4]. The field of BEEM quickly extended to buried semiconductor heterostructures including heterojunction band offsets, hot-carrier transport and resonant tunneling through double barrier and superlattice heterostructures. Further research was also performed on low-dimensional nanostructures such as quantum wires and quantum dots, as well as imaging buried structural defects such as dislocations and point defects [5–7]. BEEM has also been applied to study local transport properties through oxides in metal–insulator–semiconductor (MIS) structures [8–11].

A few excellent review articles on different aspects of BEEM have been published. Early BEEM research was reviewed in Refs. [5,12], BEEM on buried semiconductor heterostructures was discussed in detail in Ref. [6] and a comparative review of BEEM and hot-electron transistors (HET) can be found in Ref. [7]. The purpose of the present article is not to give a broad survey of the established areas in BEEM. Instead, the goal is to focus on a few emerging fields in which BEEM has made significant progress over the last few years or has demonstrated its promise as the appropriate characterization tool.

The present review is structured as follows: Section 2 reviews spin-sensitive hot-electron transport and BEEM research in magnetic thin films and multilayers; Section 3 reviews BEEM on organic materials; Section 4 reviews photon emission phenomena in BEEM and related luminescent hot-electron devices; and finally, Section 5 reviews several other promising areas including BEEM of cross-sectional semiconductor heterostructures and advanced insulator films.

1.1. BEEM transport model

The spectral shape of the BEEM current through m–s interfaces and semiconductor heterostructures can be derived from quantum mechanics and a detailed knowledge of semiconductor band structures. Two prevailing theoretical models, the Bell–Kaiser (BK) model and the Ludeke–Prietsch (LP) model, have been developed to describe the BEEM spectrum near the threshold region. They are both based on a planar tunneling formalism and the assumption of transverse momentum conservation at the m–s interface. The LP model includes the energy-dependent electron attenuation in the metal base layer and quantum mechanical transmission (QMT) at the m–s interface. Both models give a power-law behavior of the near-threshold BEEM current as a function of the extra kinetic energy,

$$I_C \sim (eV_{tip} - \phi_S)^\alpha, \tag{1}$$

where e is the electron charge, V_{tip} is the tip-to-base bias and ϕ_S is the Schottky barrier height. The scaling exponent, α differs slightly for the BK ($\alpha = 2$) and LP ($\alpha = 2.5$) models. It was found that near the threshold regime (up to ∼200 meV above the threshold), no quantitative difference between the BK and LP models can be resolved beyond the experimental error and both of them give a reasonably good fit to the experimental data. The BK model is most frequently used due to its simplicity. Deviations from this model at higher V_{tip} occur due to mechanisms including bias-dependent tunnel current distribution, scattering in the metal base and impact ionization in the semiconductor collector.

A more generalized description of BEEM must take into consideration the four distinct regions shown in Fig. 2. (1) The tunneling probability, $D(E_z)$ for an electron from the STM tip to the metal base; (2) the hot-electron transmission, $R(E)$ through the metal base characterized by an attenuation factor $R = $ constant (BK) or $R(E) = \exp[-d/\lambda(E)]$ (LP), where d is the thickness of the base and $\lambda(E)$ is the energy-dependent attenuation length; (3) the transmission probability, $C(E)$ across the m–s interface, which is either approximated as a step function (BK) or $C(E) \sim \sqrt{\frac{2m^*}{\hbar^2}(E - \phi_S) - k_\parallel^2}$ (LP), where m^* is the electron effective mass in the semiconductor, and $k_\parallel$ is the transverse component of electron momentum (parallel to the interface); (4) the transmission probability, $S(E)$ across the semiconductor heterostructure, first introduced by Smith and Kogan (SK model) [13]. Steps (3) and (4) can be combined into an overall transmission coefficient, $T(E)$ across the m–s interface and the buried heterostructure with a transfer matrix method [7]. In these terms, the total collector current in the extended BK model can be written as [7]

$$I_C(V_{tip}) = RI_{tip} \frac{\int_{E_z^{min}}^{\infty} dE_z D(E_z) T(E_z) \int_0^{E_\parallel^{max}} dE_\parallel [f(E) - f(E + eV_{tip})]}{\int_0^{\infty} dE_z D(E_z) \int_0^{\infty} dE_\parallel [f(E) - f(E + eV_{tip})]}, \tag{2}$$

where I_{tip} is the tip tunnel current. The integral limits $E_z^{min} = E_f - eV_{tip} + \phi_S$ and $E_\parallel^{max} = \frac{m^*}{m_0 - m^*}(E_z - E_f + eV_{tip} - \phi_S)$ are due to the conservation of the total energy and transverse momentum of electrons at the m–s interface. Here, E_f is the Fermi energy and m_0 is the free electron mass.

1.2. BEEM resolution

Transverse momentum conservation at the m–s interface has been traditionally used to account for BEEM resolution. Due to the much smaller electron effective mass in the semiconductor and the potential step (Schottky barrier) at the interface, the transverse momentum conservation implies that an electron refraction effect exists at the interface. As a result, only electrons with their angle of incidence smaller than a critical acceptance angle can be
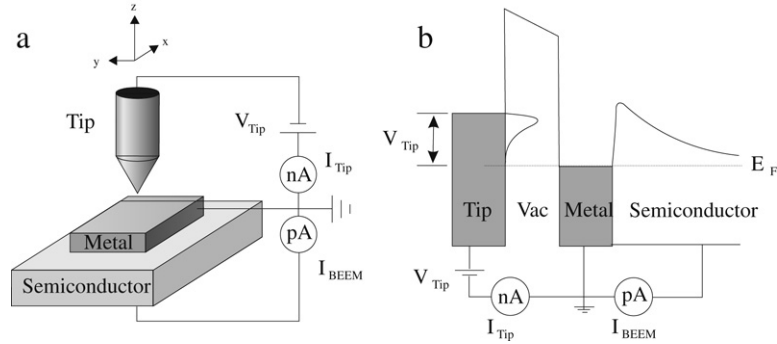
Fig. 1. (a) Schematic diagram of the experimental setup for BEEM and (b) the corresponding energy band diagram.
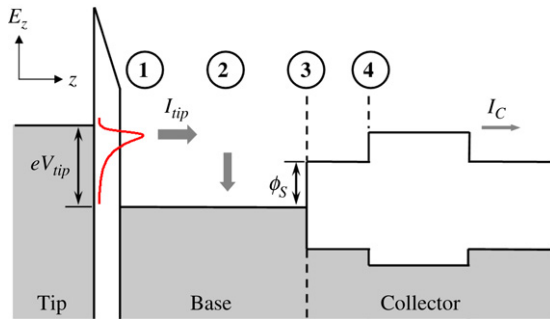

Fig. 2. Schematic of hot-carrier transport phenomena involved in theoretical modeling of BEEM. Four distinct transport regions exist in this system. (1) Tunneling from the STM tip to the metal base, (2) propagation (attenuation) in the metal base, (3) transmission at the m–s interface and (4) transmission at the buried heterojunction interface.

collected into the semiconductor. Those scattered electrons with a larger angle of incidence will be reflected at the interface and not contribute to the collector current. The critical acceptance angle, θ_C is obtained from [3]

$$\sin^2(\theta_C) = \frac{m^*}{m_0} \frac{eV_{tip} - \phi_S}{eV_{tip} + E_f}. \tag{3}$$

For the Au–GaAs interface, the calculated θ_C is only a few degrees. Since hot electrons initially tunneling into the base are highly focused in the forward direction, the small acceptance angle essentially acts as a filter that allows only ballistic electrons to be collected. Scattering in the base layer usually does not deteriorate the lateral resolution, but rather less collector current is measured. This is in large contrast to a solid-state all-semiconductor HET device in which no such large effective-mass mismatch exists.

The transverse momentum conservation originates from the translational symmetry in the plane; therefore, for nonepitaxial m–s interfaces transverse momentum may not be strictly conserved. For example, BEEM on Au/GaAs(001) found that the contribution from the L valley, consisting of states with substantial transverse wavevectors, is actually much greater than that from the Γ valley [14]. To explain this discrepancy, the m–s interface induced scattering (MSIS) model was proposed [15]. This model includes the anisotropic nature of the electron effective mass. It was found that scattering at the m–s interface can redistribute the injected electron flux so that valleys with zero interface transverse wavevector are not preferentially weighted. The BEEM data on Au/Si and Au/GaAs systems are adequately described only in the strong scattering limit. This was further confirmed by secondary-derivative BEEM spectra on Au/GaAs/Al$_x$Ga$_{1-x}$As single-barrier systems [16].

In general, interfacial scattering is undesirable because it deteriorates the spatial resolution of BEEM. However, for specific hot-electron devices, such as integrated thermionic energy converters, complete nonconservation of transverse momentum is preferred to achieve the highest possible thermoelectric power factors [17,18].

Experimentally, the observed lateral resolution of BEEM has been found to be as small as 1 nm at the m–s interface after hot electrons traverse a Au base with a thickness of 10 nm [6]. BEEM imaging on epitaxially-grown CoSi$_2$/Si structures have proven the ability to obtain atomic resolution [19]. This was attributed to an electron focusing effect resulting from the silicide band structure.

2. Magnetic thin films

The study of magnetic thin films with BEEM is partially fueled by the great success of spintronic (spin-based electronics) devices which rely heavily on the intrinsic properties of magnetic thin films. Spintronic technology exploits the charge as well as the spin degree of freedom of the electron. These devices have the potential of being faster and consuming less energy than conventional devices [20–22]. Past research of magnetic thin films has led to the development of successful spintronic devices. Most notable was the discovery of giant magnetoresistance (GMR) [23,24]. GMR is the large change in electrical resistance of certain multilayered structures in the presence of an external magnetic field. The application of this phenomenon in hard drive read heads resulted in a dramatic increase in storage capacity. The mechanism that makes magnetoresistive devices possible is spin dependent scattering in ferromagnetic (FM) materials. Spin dependent scattering arises from the imbalance in the density of states (DOS) between the spin-minority and spin-majority carriers due to the difference in the energy associated with the two spin species of carriers in the presence of a magnetic field [25]. Minority electrons have a larger number of empty states to decay into than do the majority electrons. Thus, according to Fermi's golden rule, the probability of scattering is greater for the minority electrons than for the majority. The difference in the DOS also creates an imbalance of spin electrons. This imbalance can be quantified in terms of the polarization, $P = (N_+ - N_-)/(N_+ + N_-)$, where N_+ is the number of majority electrons in the system and N_- is the number of minority electrons. When the DOS is composed entirely of electrons of one type of spin orientation that material is said to be 100% spin polarized.

The GMR spin valve consists of two FM metals sandwiching a non-FM metal. Changing the magnetic alignment of the two FM metals causes the DOS of the spin populations in one metal to change relative to the other. This causes a change in the resistance of the structure, a minimum resistance when the magnetic alignment is parallel (P) and a maximum resistance when it is anti-parallel (AP). The quality of a magnetoresistive device can be gauged by the magnetoresistance ratio (MR), defined as
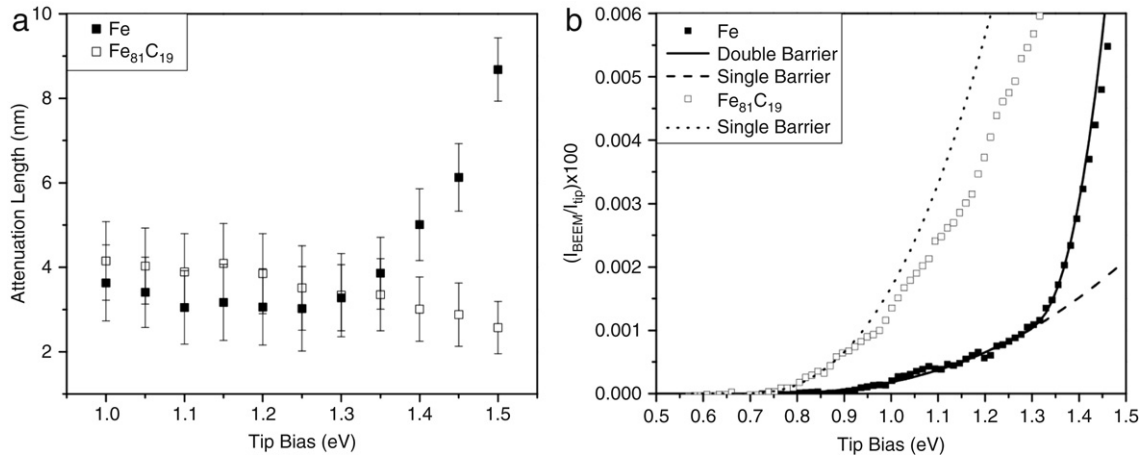
Fig. 3. (a) The ballistic attenuation lengths as a function of tip bias for $Fe_{81}C_{19}$/Si(001) and Fe/Si(001) Schottky diodes. (b) Examples of BEEM spectra obtained from these diodes. Note the second threshold voltage in the spectra of the Fe films at 1.29 eV corresponding to the sharp increase in the energetic dependence of its attenuation length seen in (a). Reprinted with permission from Ref. [33].
© 2006, American Physical Society.

$(R_P - R_{AP})/(R_{AP}) \times 100$, where R_P is the parallel resistance and R_{AP} is the anti-parallel resistance. Typically, the percentage change in MR for a GMR read head is 10%–20%, which is much greater than the 3% achieved in anisotropic magnetoresistive read heads used previously. Currently, GMR devices are being superseded by magnetic tunneling junction (MTJ) devices for hard drive read heads. MTJs use an insulator as the spacer layer between the FM metals and exhibit an even higher MR of 20%–30% [26–28].

The following section on spin dependent transport is limited by the scope of this review article. An enormous amount of research has been performed in the field of spintronics, both experimental and theoretical. The interested reader should refer to the reviews that have been previously published (see for example Refs. [20,29–31]).

2.1. Unpolarized ballistic electron transport

Before understanding spin-polarized electron transport in magnetic thin films, it is first useful to examine hot-electron transport in a single FM layer without discrimination of their spin degree of freedom. One way to quantify hot-electron transport is by measuring the attenuation length, λ. This is done by measuring the BEEM current, I_C through a Schottky diode, as a function of metal thickness and tip bias. The effective attenuation length through the diode can then be obtained from

$$I_C(d, V_{tip}) = I_C(d = 0, V_{tip})e^{(-d/\lambda)}. \qquad (4)$$

Here $I_C(d = 0, V_{tip})$ is a proportionality constant.

Recently, this method has been utilized on magnetic thin films such as Co, Fe, FeC, Ni and NiFe yielding ballistic attenuation lengths ranging from 0.3 to 4.1 nm at room temperature [32–35].

BEEM spectra acquired on MnSi/Si(001) Schottky diodes at 80 K displayed two threshold voltages at 0.71 ± 0.01 eV and 0.86 ± 0.02 eV [36]. The second threshold is attributed to the existence of an additional conduction band minimum (CBM) in the band structure at the MnSi/Si(001) interface. This was unexpected since additional CBM is not present in the bulk Si band structure in this energy range [37], nor are they observed in BEEM experiments using more ideal metals such as Au. Additional CBMs were theoretically predicted in the $NiSi_2$/Si(001) system but have not been observed in experimental BEEM studies, possibly due to scattering in the silicide [38–40]. A study of Au/Fe/Si(001) Schottky diodes at 80 K also found an additional threshold voltage in the BEEM spectra occurring at 1.29 ± 0.04 eV [33]. The additional CBM

associated with the second threshold was previously predicted and attributed to metal induced gap states (MIGS) resulting from the poor coordination of dangling d bonds at the Fe interface layer with the Si [41]. It is unlikely that this extra threshold is from a thin FeSi alloyed layer since there was no annealing step after deposition and the bandgap of such a layer would only be 0.13 eV [42]. The addition of 19% C to the Fe films was found to suppress the additional threshold voltage. The addition of C possibly eliminates the dangling bonds of Fe as well as the MIGS.

The energetic dependence of the attenuation length measured on Au/Fe/Si(001) and Au/FeC/Si(001) Schottky diodes is shown in Fig. 3(a). The attenuation lengths measured on the Au/FeC/Si(001) diodes decrease monotonically with energy in this energy range, consistent with electron–electron scattering. In contrast, the Au/Fe/Si(001) diodes exhibited a dramatic increase in the effective attenuation length at approximately 1.3 eV. This increase coincides with the onset of the second threshold voltage in the Au/Fe/Si(001) BEEM spectra at 1.29 eV seen in Fig. 3(b). The CBM associated with the second threshold voltage has a larger number of available transverse momentum states with greater transverse momentum than the CBM associated with the Schottky threshold. The larger number of available states makes the BEEM current less sensitive to electrons elastically scattered in the Fe film, causing an increase in the effective attenuation length in these diodes. A second threshold voltage was not seen in the Au/FeC/Si(001) Schottky diodes (see Fig. 3(b)).

2.2. Spin-polarized ballistic electron transport

The past success of BEEM to study non-polarized hot-electron transport makes it an ideal technique to study spin-polarized electron transport. There are two different categories of BEEM techniques: the first is based on the STM setup, while the second makes use of planar tunneling devices. This section will describe how both of these methods have been modified to study spin-polarized transport as well as some of the more significant results.

2.2.1. STM-based techniques

In order to take advantage of the nanoscale positioning of the STM scanner, Rippard et al. modified the BEEM technique to perform ballistic electron magnetic microscopy (BEMM) [43]. In BEMM, a thin film stack is grown on a semiconductor substrate consisting of two FM metal layers decoupled by a non-FM spacer layer. Using the BEEM setup, electrons are injected from the STM
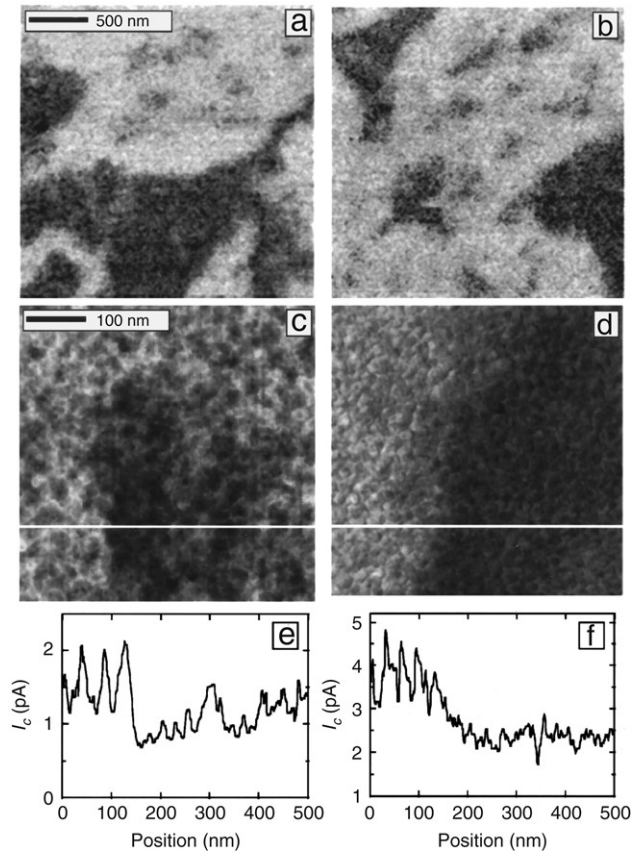
Fig. 4. BEMM image of sputtered Au/Cu/Co/Cu/Co/Cu/Au structures on Si(111) at $H = 30$ Oe (a) and after H has been reduced to 0 Oe (b). 500×500 nm^2 BEMM images of similar (c) sputtered and (d) evaporated films. The cross-sectional plots of the white lines in (c) and (d) are shown below their respective images in (e) and (f). $V_{tip} = 1.5$ eV and $I_{tip} = 4$ nA. Reprinted with permission from Ref. [44].
© 2000, American Institute of Physics.

Fig. 5. (a) BEMM spectra recorded on Au/NiFe/Cu/Co/GaAs(001) using a tunneling current of 20 nA at $H = 0$ Oe and $H = 26$ Oe corresponding to parallel and anti-parallel alignment, respectively. (b) Collector current measured as a function of magnetic field for $V_{tip} = 1.5$ eV and $I_{tip} = 20$ nA at room temperature. Reprinted with permission from Ref. [45].
© 2004, American Institute of Physics.

tip into the first FM metal where they become polarized. This occurs due to an asymmetry in the scattering rate of the two spin species in the film as well as spin dependent reflections at the interface. Similar to the GMR effect, the amount of spin dependent scattering in the second FM metal depends on its magnetic alignment with the first. Essentially, the first FM metal acts as the polarizer while the second FM metal plays the part of the analyzer. This effect gives BEMM magnetic contrast and has provided some interesting images of magnetic domains on Co/Cu/Co [43,44] as well as on Co/Cu/NiFe [45] stacks.

Images in Fig. 4 demonstrate the ability of BEMM to image magnetic domains of Au/Cu/Co/Cu/Co/Cu/Au structures on Si(111) at room temperature. These structures typically exhibited domain walls with widths of 100–200 nm. Fig. 4(a) and (b) show how the domains change as the magnetic field is reduced from 30 to 0 Oe on sputtered films. The transition of these domains from P alignment to AP alignment was found to occur over a variety of lengths from ∼10 nm to several hundred nanometers, as seen in the sputtered films (Fig. 4(c) and the corresponding line scan in (e)) and in the evaporated films (Fig. 4(d) and its corresponding line scan in (f)), respectively.

In addition to magnetic imaging, BEMM can also be utilized to perform spectroscopy. Fig. 5(a) demonstrates the change in the spectra with and without an applied external field of 26 Oe on a Au/NiFe/Cu/Co/GaAs(001) sample at room temperature using a tunneling current of 20 nA. By measuring the BEMM current as a function of applied external field, it is possible to measure a BEMM hysteresis loop [45,46]. The hysteresis occurs due to
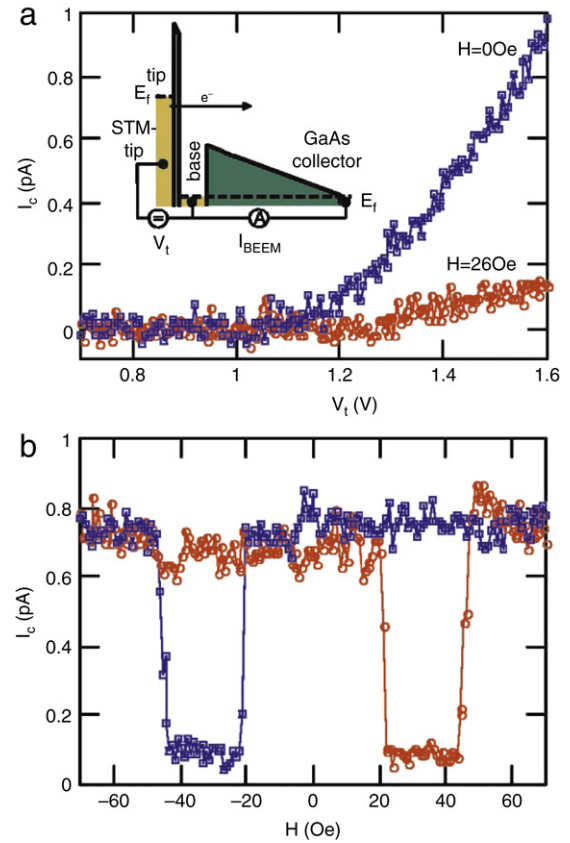
a difference in the coercivity of the two FM metals in the trilayer stack. An example of such a hysteresis loop is shown in Fig. 5(b) for Au/NiFe/Cu/Co/GaAs(001). For both polarities the BEMM current reaches a minimum between ∼20 and ∼40 Oe. As the field increases beyond 40 Oe, the two FM layers are forced into P alignment resulting in a higher BEMM current. The magnetocurrent (MC) can be determined from such hysteresis loops. The MC is defined in terms of the BEEM current in P and AP alignment as $(I_{C,P} - I_{C,AP})/(I_{C,AP}) \times 100$. Various types of spin valves have been studied in this manner yielding MCs ranging from 400%–600% [45,46].

The effective spin dependent attenuation lengths have been determined by measuring the BEMM current in P and AP alignment on Co/Cu/Co/Cu/Au/Si(111) Schottky diodes as a function of the thickness of the second Co layer [47]. This was accomplished in a similar manner as the unpolarized attenuation lengths; however, Eq. (4) is insufficient to describe a two current system. In order to properly model the BEMM current in P and AP alignment, the following equations are used [47]:

$$I_{C,P} = I_o[f_+ T_{o+} T_{i+}^* T_{o+}^* e^{(-d_1/\lambda_+)} e^{(-d_2/\lambda_+)} + f_- T_{o-} T_{i-}^* T_{o-}^* e^{(-d_1/\lambda_-)} e^{(-d_2/\lambda_-)}], \tag{5}$$

$$I_{C,AP} = I_o[f_+ T_{o+} T_{i-}^* T_{o-}^* e^{(-d_1/\lambda_+)} e^{(-d_2/\lambda_-)} + f_- T_{o-} T_{i+}^* T_{o+}^* e^{(-d_2/\lambda_+)} e^{(-d_1/\lambda_-)}]. \tag{6}$$

Here I_o is the overall scaling factor, $f_{+(-)}$ is the fraction of majority (minority) electrons in the initial tunneling current due to the

splitting of the spin dependent DOS in the first Co film, $\lambda_{+(-)}$ is the effective majority (minority) attenuation length in the Co films, $T_{o(i)+(-)}$ is the transmission coefficient out of (into) a Co layer for the majority (minority) electrons, $d_{1(2)}$ is the Co thicknesses of the first (second) layer. The * indicates the second Co layer beneath the Cu film. Fitting these equations to the data, the effective spin dependent attenuation lengths for Co at 300 K were extracted yielding values of $\lambda_+ = 2.1 \pm 0.1$ nm and $\lambda_- = 0.83 \pm 0.08$ nm at a tip bias of $V_{tip} = 1.5$ eV. These values indicate that the minority electrons are being scattered at a rate approximately 2.5 times greater than the majority electrons.

Spin flip scattering acts to randomize the spin orientation of a current. This process would tend to reduce the polarization of the current and have a detrimental effect on spintronic devices. Perrella et al. studied the change in polarization due to the effects of electron–electron scattering in the spacer layer of Co/Cu/Al/Cu/Co/Cu/Au/Si(111) Schottky diodes using previously measured attenuation lengths in Co [48]. Knowing the spin dependent attenuation lengths allows the polarization of ballistic electrons exiting the first Co to be calculated as a function of the film thickness from

$$P_{in} = \frac{e^{-d/\lambda_+} - \alpha e^{-d/\lambda_-}}{e^{-d/\lambda_+} + \alpha e^{-d/\lambda_-}}, \qquad (7)$$

where α is a transmission coefficient for the first Co/Cu interface. The polarization of the current exiting the spacer layer can be determined by using the current measured in the P and AP alignments in the equation

$$P_{out} = \frac{e^{-d/\lambda_+} + \beta e^{-d/\lambda_-}}{e^{-d/\lambda_+} - \beta e^{-d/\lambda_-}} \left(\frac{I_{C,P} - I_{C,AP}}{I_{C,P} + I_{C,AP}} \right), \qquad (8)$$

where β is a transmission coefficient for the second Cu/Co interface. The amount of electron–electron scattering was controlled by adjusting the O_2 content in the Al layer. Fig. 6(a) shows the polarization of the BEMM current coming out of the Cu/Al/Cu spacer layer as a function of O_2 dose at a tip bias of $V_{tip} = 2.0$ eV. The dashed line indicates the polarization of the electrons exiting the first Co film as well as the polarization of the BEMM current with no O_2 exposure. An obvious decrease in polarization is seen as the O_2 content (i.e. the amount of electron–electron scattering) increases. Fig. 6(b) shows the polarization out of the spacer layer as a function of the maximum BEEM current. The decrease in polarization with decreasing current provides direct evidence that scattering which causes a loss of signal also causes a loss of polarization.

Spin-polarized tunneling with STM was demonstrated nearly two decades ago utilizing an FM metal tip to inject spin-polarized carriers [49]. Recently, such tips were used in a three-terminal BEEM configuration to study spin-polarized ballistic transport through FM metal overlayers on semiconductor substrates [50]. This technique has the advantage of requiring only a single FM metal film grown on a semiconductor rather than a more complicated multilayered stack, greatly simplifying Eqs. (5) and (6),

$$\frac{I_{C,P\,(AP)}}{I_{tip}} = \frac{C_+}{2}(1 + (-)P_o)e^{-d/\lambda_+} + \frac{C_-}{2}(1 - (+)P_o)e^{-d/\lambda_-}. \qquad (9)$$

Here P_o is the initial polarization of the electrons tunneling from the FM tip and $C_{+(-)}$ takes into account the non-thickness dependent scattering (i.e. interface scattering) of majority (minority) electrons.

Thickness dependent BEEM using an Fe-coated Au tip was performed on Au/Fe/Si(001) Schottky diodes at 80 K yielding attenuation lengths of 2.5 ± 0.3 nm for the majority and 1.8 ± 0.2 nm for the minority electrons at a tip bias of 1.5 eV. Similar to the unpolarized case [33], the majority attenuation length exhibited a substantial increase after the onset of the second
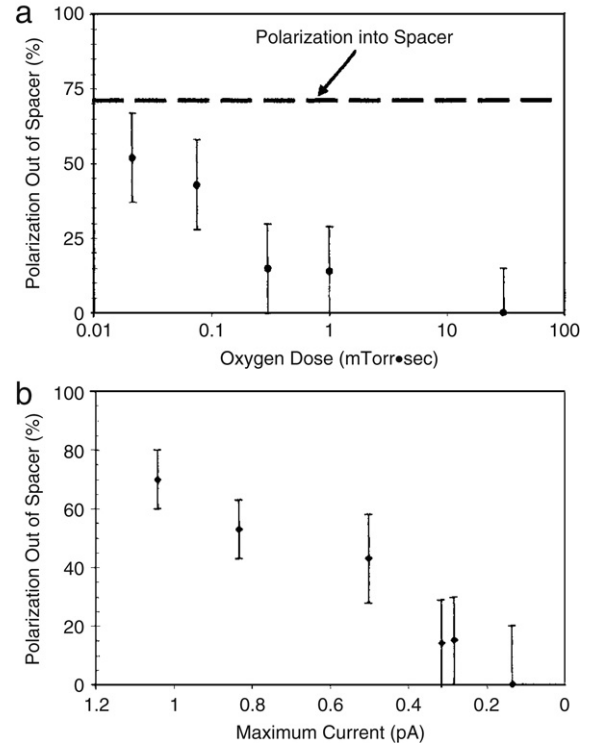

Fig. 6. (a) The electron polarization exiting the spacer layer of Co/Cu/Al/Cu/Co/Cu/Au/Si(111) samples as a function of the oxygen dose in the Al film. The horizontal line at 71% indicates the polarization entering the spacer layer as well as the polarization measured when the spacer layer is entirely Cu or when the Al is not exposed to oxygen. (b) The polarization exiting the spacer layer as a function of the maximum current at a tip bias of 2.0 eV. Reprinted with permission from Ref. [48]. © 2005, American Institute of Physics.

threshold voltage at 1.29 eV. This was also observed in the minority electrons to a lesser degree. The increased attenuation length beyond the second threshold is due to the collection of electrons with large transverse momentum. Minority electrons that undergo high elastic scattering rate in the metal have a broader momentum distribution at the m–s interface. Therefore the effect of increased transmission is less prominent.

2.2.2. Planar tunneling techniques

An alternative to STM-based BEEM techniques is to use planar tunneling devices such as the metal-based hot-electron transistor. Rather than injecting electrons by means of a STM tip, the hot electron transistor uses a planar solid-state tunnel junction to inject hot electrons ballistically through a metal base layer into a semiconductor collector. The magnetic tunneling transistor (MTT) is a modified hot-electron transistor that utilizes an MTJ to inject spin-polarized electrons ballistically through an FM metal base layer into a semiconductor collector [51,52].

Though incapable of magnetic imaging like its BEMM counterpart, MTTs are capable of performing spectroscopic analysis of FM metals. Thickness dependent studies of NiFe in Ta/IrMn/CoFe/Al$_2$O$_3$/NiFe/GaAs(001) MTTs at 77 K have given values of 6.7 ± 0.26 nm for the majority and 1.3 ± 0.1 nm for the minority electron attenuation lengths [53]. Extrapolation of the MC measured in these samples reveals that it approaches zero at zero thickness. This indicates that spin dependent scattering between the NiFe and the GaAs(001) is negligible. In a similar experiment, when CoFe was used in place of NiFe, it was uncertain if the MC went to zero, making it impossible to rule out spin dependent scattering at the interface [53].
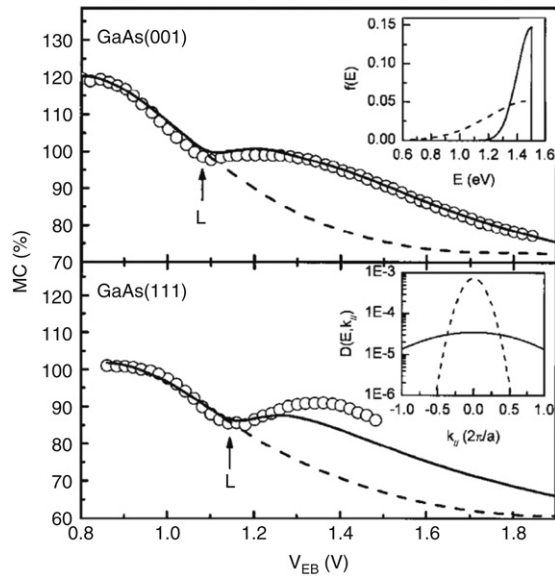
Fig. 7. Bias dependence of the MC for Ta/IrMn/CoFe/Al$_2$O$_3$/CoFe on both GaAs(001) (top) and GaAs(111) (bottom) MTTs. The solid lines represent the calculated MC assuming a large angular distribution. The dashed lines represent the same calculation except for a smaller angular distribution. The arrows indicate the onset of electron transmission into the GaAs L conduction band valley. The upper and lower insets show a narrow and broad electron energy distribution function and electron angular distribution function at V_{EB} = 1.5 eV, respectively. Reprinted with permission from Ref. [54].
© 2003, American Physical Society.

The MC of Ta/IrMn/CoFe/Al$_2$O$_3$/CoFe/GaAs MTTs on both GaAs(001) and GaAs(111) substrates seen in Fig. 7 exhibit a nonmonotonic dependence on the emitter bias at 77 K. At an emitter bias of approximately V_{EB} = 1.1 eV both structures display a change in the energetic dependence of the MC as the L conduction band opens. This dependence has also been seen on other GaAs-based MTTs and indicates that the band structure of the metal/GaAs interface is affecting spin transport in these devices [54,55]. This behavior can be predicted using the model developed for BEEM [56,15,57]. Taking spin dependent effects into account, the collector current can be written as [54]

$$I_{C,P(AP)} = I_E(0.5 + 0.5P_E)\exp(-d/\lambda_{+(-)})$$
$$\times \int_{\phi_S}^{eV_{EB}} f_{+(-)}(E) \int D(E, k_\parallel)T(E, k_\parallel)dk_\parallel dE$$
$$+ I_E(0.5 - 0.5P_E)\exp(-d/\lambda_{-(+)})$$
$$\times \int_{\phi_S}^{eV_{EB}} f_{-(+)}(E) \int D(E, k_\parallel)T(E, k_\parallel)\, dk_\parallel dE, \quad (10)$$

where I_E is the tunnel current injected from the emitter into the base, P_E is the injection polarization, d is the thickness of the base layer, $\lambda_{+(-)}$ is the majority (minority) attenuation length in the base layer, ϕ_S is the Schottky barrier height, $f_{+(-)}$ is the distribution function for the majority (minority) electrons at the m–s interface, D is the angular distribution of the electrons due to scattering in the base layer, T is the transmission probability at the m–s interface, and $k_\parallel$ is the momentum vector parallel to the sample surface. It should be noted that the attenuation lengths in this equation are not the effective attenuation lengths measured using BEEM, rather they are the attenuation lengths inside the FM metal base.

The upper inset of Fig. 7 shows the electron energy distribution for a large (dashed line) and small (solid line) amount of scattering, representative of the minority and majority electrons, respectively. Because the spin asymmetry is greatest for energies closest to eV_{EB}, the maximum MC collected through the narrow Brillouin

zone centered (Γ point) conduction band in GaAs is obtained when the electrons are collected with a minimum energy loss ($eV_{EB} \approx \phi_S$). As the emitter bias increases, inelastic scattering of electrons will be less likely to remove these electrons from the collector current, causing a decrease in the MC. The same is also true as electrons begin to access the L valley conduction band. The increase in the MC seen at $V_{EB} \approx 1.1$ eV indicates a large contribution to the current from electrons propagating in the L valley. The lower inset shows a broad (solid line) and narrow (dashed line) angular distribution. Because all or six out of eight L valley ellipsoids (for the GaAs(001) and GaAs(111) substrates, respectively) are centered at large transverse wavevectors, the large contribution of the L valley to the collector current can only be explained if the electrons have a large angular distribution at the CoFe/GaAs interface (solid lines). Indeed, when a narrow distribution is assumed, a monotonic dependence is seen (dashed lines). The slight difference in the shape of the emitter bias dependence of the MC on the GaAs(001) and GaAs(111) substrates is attributed to structural differences on the two different facets.

In general, MTTs have only exhibited a moderate MC of approximately 100% [53,58]. One notable exception is a modified MTT developed by Van Dijken et al. that uses a nonmagnetic tunneling junction to inject electrons into a GMR spin valve base [59]. This structure consists of Cu/Al$_2$O$_3$/NiFe/Cu/CoFe/GaAs(001) and exhibits a MC of more than 3400% at $V_{EB} \sim 0.8$ eV at 77 K. More important, from a device standpoint, was the large collector current (~ 7.5 μA) measured at V_{EB} = 2.5 eV while still maintaining a MC of 670%. It is not expected that the MC would change significantly at room temperature since only a moderate MC temperature dependence has been observed [60].

The solid circles in Fig. 8(a) show the MC of this device as a function of FM layer thickness. The open circles show the corresponding effective transmission polarization at an emitter bias of V_{EB} = 1.5 eV. The effective transmission polarization is calculated from the MC by $P = \sqrt{MC/2 + MC}$. The rapid increase in transmission polarization occurs due to the relatively large asymmetry in the spin dependent scattering inside the FM layers. The saturation of the P at $\sim 95\%$ for FM layer thicknesses greater than 5 nm is an indication that the maximum polarization of this structure is limited by spin flip scattering events at the interfaces of the films.

The emitter bias dependence of the MC is shown in Fig. 8(b) for a structure with a 5 nm thick NiFe layer. At higher emitter biases inelastic scattering of electrons will be less likely to remove these electrons from the collector current, causing the decrease in the P with emitter bias. Fig. 8(c) and (d) depict the difference in the electron energy distribution for P and AP alignments of the FM metals.

Previous studies of spin transport inside semiconductors have been primarily limited to direct-bandgap semiconductors due to the need to measure the photon polarization after spin injection [61,62]. Recently, it has been shown that spin transport in Si can be studied electrically using modified MTTs [63–67]. These MTTs utilize an undoped single crystal Si spacer layer between two FM layers. The dependence of the collector current on the relative magnetization of the FM layers indicates that spin coherence is maintained in Si layers to at least 350 μm. Spin precession in a perpendicular magnetic field was studied with these devices by measuring the oscillations in the collector current as a function of the applied magnetic field. The average spin transit time, τ is related to the period of these oscillations, $2B_\pi$ by $\tau = h/(2g\mu_B B_\pi)$. Here, g is the electron spin g factor and μ_B is the Bohr magneton. Knowing the spin transit time allows the spin lifetime, T_1 to be calculated from the magnetocurrent using a simple exponential decay relationship,

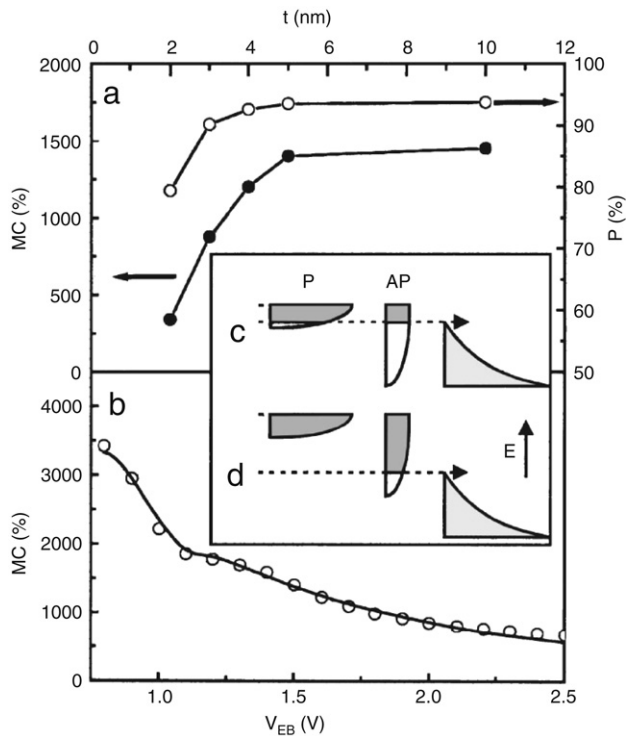$$MC/(MC + 2) \propto e^{-\tau/T_1}. \quad (11)$$

Fig. 8. (a) The FM layer (CoFe and NiFe) thickness dependence of the MC (solid circles) of $Cu/Al_2O_3/NiFe/Cu/CoFe/GaAs(001)$ MTTs and the corresponding effective transmission polarization of the FM layers (open circles) for an emitter bias of 1.5 eV. (b) Emitter bias voltage dependence of the MC for a MTT with FM layer thickness of 5 nm (open circles). The solid line represents the theoretical fit. The difference in electron energy distribution for parallel and anti-parallel alignment of the base magnetic moments is illustrated for small (c) and large (d) emitter bias voltage. Reprinted with permission from Ref. [59].
© 2003, American Institute of Physics.

Shown in Fig. 9(a) is the normalized MC obtained from a MTT with a 350 μm Si spacer layer as a function of transit time at device temperatures ranging from 60 to 150 K. The transit times were determined from spin precession experiments in a perpendicular magnetic field. The solid lines represent fits to Eq. (11). The resulting spin lifetimes determined from these fits are plotted as a function of temperature in Fig. 9(b) as well as a comparison to Yafet's $T^{-5/2}$ power law for indirect-bandgap semiconductors [68]. These show that this technique holds promise for studying spin injection in a wide variety of indirect-bandgap semiconductors.

2.3. Spin-polarized ballistic hole transport

While much research has been devoted to the study of spin-polarized electron transport in magnetic thin films using BEEM-based techniques, little work has been done to study spin-polarized holes. If holes are able to transverse interfaces without the loss of spin polarization then spintronic devices based on hole injection into p-type semiconductors can be realized. To this end, ballistic hole magnetic microscopy (BHMM) was developed to study spin hole transport [69]. In BHMM, hot holes are injected from a STM tip into a spin valve structure on a p-type semiconductor using a positive tip bias. In this manner the amount of hole current can be measured in P and AP alignment.

The top panel of Fig. 10 shows a clear change in the amount of hole current for P ($H = 100$ Oe) and AP ($H = -30$ Oe) alignment acquired at 150 K on Au/Co/Au/NiFe/Au/p-Si(001) Schottky diodes indicating that spin dependent scattering is occurring. This is further reinforced by the BHMM hysteresis loop shown in the
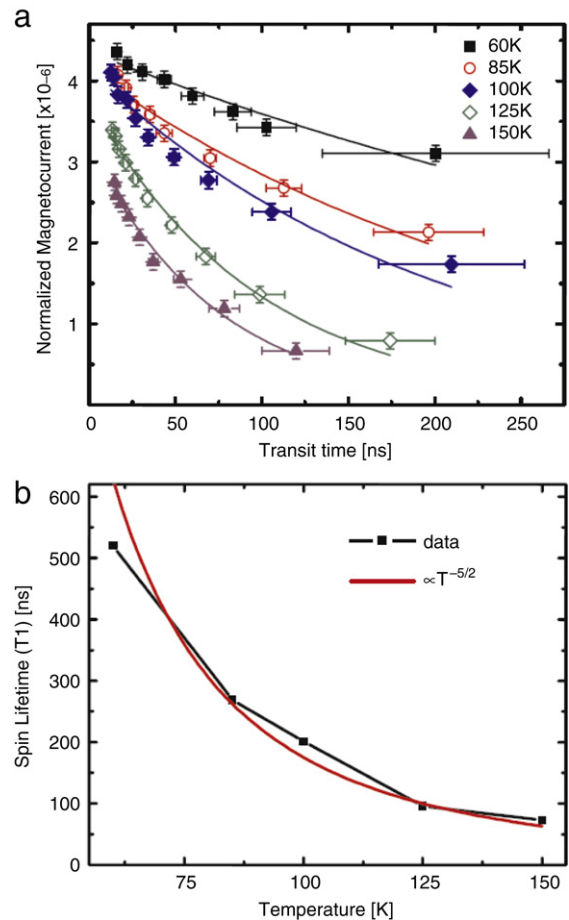
Fig. 9. (a) Fits of the normalized magnetocurrent using Eq. (11) to the spin transit time in a MTT with a 350 μm Si spacer layer. (b) The experimental spin lifetime as a function of device temperature compared to Yafet's $T^{-5/2}$ power law. Reprinted with permission from Ref. [65].
© 2007, American Physical Society.

bottom panel of Fig. 10, acquired at a tip bias of $V_{tip} = 2$ eV and a 10 nA hole injection current. This structure was found to exhibit a MC of 130%. The large dependence of the hole current on the magnetic alignment was unexpected for these samples, since there is little difference in the number of final states into which a hot hole in the majority and minority spin bands can decay just below the Fermi level in Co [69]. The spin dependent scattering is explained by taking into account the difference in group velocity in the states in which the two different spin holes can propagate [69]. The inset of Fig. 10 shows the partial density of s, p like states for Co in the face-centered-cubic (FCC) phase. The decrease in the majority states just below E_F results in a smaller velocity of these holes, increasing the time they spend in the FM metal. This in turn gives them more opportunities to undergo inelastic scattering. This hypothesis suggests that the current due to holes traveling in the minority band is greater than that of the majority band, the opposite of what is observed for electrons. It would be interesting if temperature dependence were studied.

To further complicate our understanding of spin-polarized holes, both negative and positive MCs were measured on NiFe/Al₂O₃/Co/Si p-type MTTs as a function of Co thickness as well as hole energy [70]. In many cases a crossover from negative to positive MC was measured for both thickness and emitter bias dependence. The measurement of a negative MC is consistent with the proposal that the current in Co due to holes traveling in the minority band is greater than those in the majority band [69]. It was found that the negative MC tended to occur in thinner Co films
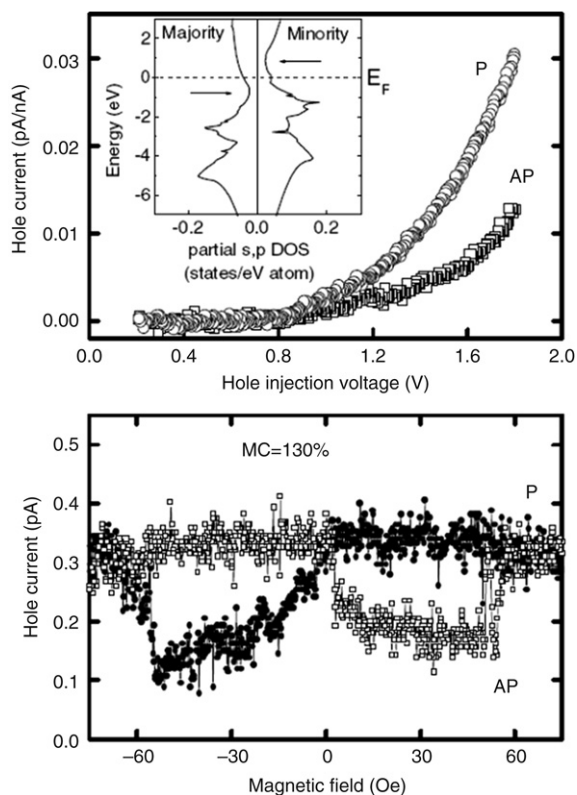
Fig. 10. (Top panel) Hole current as a function of tip bias on Au/Co/Au/NiFe/Au/p-Si(001) for P ($H = 100$ Oe) and AP ($H = -30$ Oe) alignment. Inset in this panel shows the s, p partial density of states for FCC Co. The arrows indicate the pronounced dips near the top of the d bands. (Bottom panel) Hole current as a function of applied magnetic field at a tip bias of 2 V and 10 nA hole current. Reprinted with permission from Ref. [69].

© 2005, American Physical Society.

where elastic scattering dominated. The crossover to positive MC occurred in thicker films where inelastic scattering dominated.

By using BHMM in reverse mode it was found that higher transmission currents could be obtained [71]. In reverse mode, the injected hot electrons from the STM tip decay inelastically via electron–hole pair excitation. The holes created from this process are then transmitted through the sample and enter the valence band of the p-type semiconductor [72]. The higher transmission currents made imaging possible on Au/Co/Au/NiFe/Au/p-Si samples [71].

Transmission rates of hot electrons/holes in the studies in this chapter are significantly limited by scattering processes within the layers and at metal–metal interfaces due to disorder and band-structure mismatches. Epitaxial base layers may reduce the elastic-scattering rate in the films compared to polycrystalline ones, increasing the BEEM current. In addition, the use of epitaxial thin films as the base layer has proven to be beneficial for improving spatial resolution of BEEM due to the electron focusing effect from the specific band structure of the metal film [19]. BEEM on epitaxial FM thin films requires a complex *in situ* fabrication in a dedicated ultrahigh vacuum (UHV) chamber due to contamination issues. Very few spin transport measurements have been carried out using BEEM-based techniques on epitaxially-grown FM films (see for example Ref. [73]). This, however, leaves much room for further research in this field.

3. Organic thin films and molecules

Organic materials (organics) are chemical compounds consisting primarily of carbon and hydrogen. With the exception of methane and its simple derivatives, most organics have multiple carbon–carbon covalent bonds and can be divided into two general classes: molecules and polymers (macromolecules composed of repeating structural units). As the basis of all life processes, organics exhibit an extremely large variety of composition, shape and chemical reactivities. The widespread industrial utilization of organics was hallmarked by the fabrication of the first synthetic organic chemical urea (carbamide, $(NH_2)_2CO$) by Wöhler in 1828 [74]. Today, artificial organics have become an indispensable part of modern civilization.

Organics have been widely employed as passive components (e.g. device packaging) in the microelectronic industry. One of the earliest applications of organics as *active* components in electronics and optoelectronics was the organic photoconductors developed for xerography in 1960s to overcome issues with amorphous selenium such as inflexibility and poor red light sensitivity [75]. In 1987, Kodak, Inc. first demonstrated an organic light-emitting device (OLED) with high luminosity which triggered tremendous commercial and scientific interest. Today, a large variety of organic electronic and optoelectronic devices are being developed including solar cells and photodetectors [76], chemical sensors [77], charge and data storage devices [78], electroluminescent devices [79], field-effect transistors (FET) [80] and nonlinear optical devices [81]. The main driving factors for replacing conventional inorganic semiconductors with organic semiconductors are their relatively low cost, integrability with established techniques, novel functionality, and flexibility. Molecular electronics is currently considered one possible solution for the continued miniaturization of microelectronics [82].

While OLEDs have found niche markets in small size displays, most of today's organic devices are still in their infant stage, plagued by practical issues such as poor conductivity and carrier mobility, non-optimized charge injection at metal contacts, and relatively short lifetime. Their performance leaves much to be desired compared with their inorganic counterparts. The success of organic-based devices calls for synergy between fundamental research and commercial development. For example, there is a poor understanding of interfacial properties between metal contacts and organics. For optimal carrier injection into organics, close energy alignment between the Fermi level of the contacting metal and the molecular orbital levels of organic molecules is needed. Electron injection into organics is generally more difficult, because it requires low-work-function alkaline metals which are susceptible to oxidation. Theoretical estimation of the energy-level alignment based on the work function difference (the Schottky–Mott rule) usually exhibits a large deviation from experimental results. Typically the energy-level alignments are deduced from conventional macroscopic spectroscopies such as current–voltage (I–V), capacitance–voltage (C–V) and internal photoemission (IPE) which average over a large device active area. These techniques are largely affected by structural inhomogeneities and local defects such as pinholes and impurities. For this reason, a local characterization is highly desirable. BEEM is a valuable tool to study organic electronic structures, charge carrier transport through organic thin films and molecules, and charge injection at metal–organic interfaces on the nanometer scale. In this section, a brief review of the recent progress made in this direction is given.

3.1. BEEM of buried organics

3.1.1. Barrier heights at metal–organic interfaces

To determine barrier heights between metals and organics, a Schottky diode can be made by depositing a metal base overlayer on an organic thin film collector. Troadec et al. studied the interface between Ag and poly(*para*-phenylene) (PPP) polymeric thin films [83]. PPP is a conjugated polymer that emits blue light
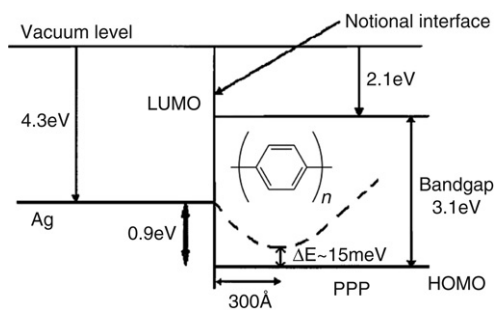
Fig. 11. Energy-level alignment for the Ag/PPP interface following the Schottky–Mott rule. Inset shows the molecular structure of PPP. The dotted line shows the Schottky barrier for hole injection after the image force potential correction. Reprinted with permission from Ref. [83].
© 2005, American Institute of Physics.

with high photoluminescence efficiency. In the form of an infinite polymer, the estimated binding energies for the highest occupied molecular orbital (HOMO) and lowest unoccupied molecular orbital (LUMO) levels of PPP measured with respect to the vacuum level are 5.2 and 2.1 eV, respectively [83]. The Schottky–Mott rule predicts that the Fermi level of Ag is aligned closer to the HOMO level than the LUMO level of PPP. For this reason, Ag is typically used to make injection-limited contacts for hole injection into PPP. A barrier height of 0.9 eV is expected between Ag and PPP as predicted by the Schottky–Mott rule (Fig. 11).

Ballistic hole emission spectroscopy (BHES) found a substantial deviation from this estimate, exhibiting nonzero current below this threshold. Note that the electronic properties (e.g. bandgap) of the PPP material depend on the length of its oligomers [84] and therefore careful structural characterization is needed to quantitatively interpret the BHES spectra. Interestingly, similar to the case of BEEM on inorganic MIS interfaces [85,86], multiple steps were found in the first derivative of the collector current (dI_C/dV_{tip}). However, it is not clear if this derivative technique can be interpreted in the same way as in the case of inorganic MIS structures. For example, Eq. (1) has been used to extract the Schottky barrier height from the raw BHES data. The best fit to their data was obtained with an exponent of $\alpha = 7/2$ and a Schottky barrier height ranging from 0.3 to 0.5 eV. The ballistic hole emission microscopy (BHEM) images exhibited substantial spatial nonuniformity of the interface transparency through the PPP films, with the relatively transparent regions several nanometers in size.

3.1.2. Organic modified metal–semiconductor interfaces

Several groups have adopted hybrid devices using organic molecules to influence and control the characteristics of conventional electronic devices. Compared with other approaches to molecular electronics, hybrid devices have several potential advantages. These include fewer limitations on the choice of molecules and relatively easy integration of molecular functionality with the scalability of established semiconductor technologies. For example, by inserting systematically varying organic molecular monolayers at m–s interfaces, interfacial properties such as the Schottky barrier height can be controlled [87]. Systematic changes in charge transport behavior across the molecularly modified junctions on the macroscale have been found by traditional spectroscopic techniques such as *I–V*, *C–V* and IPE [88].

The band profiles of these hybrid devices are somewhat similar to MIS structures extensively studied by BEEM previously, making BEEM an excellent technique to study these hybrid systems on the nanometer scale. In a study by Li et al. on Au/octanedithiol/n-GaAs(001), the molecular layer of 1, 8-octanedithiol [$SH(CH_2)_8SH$] (C8DT) took the role of an insulator sandwiched between an 8 nm Au electrode and an n-type GaAs substrate [89]. To avoid
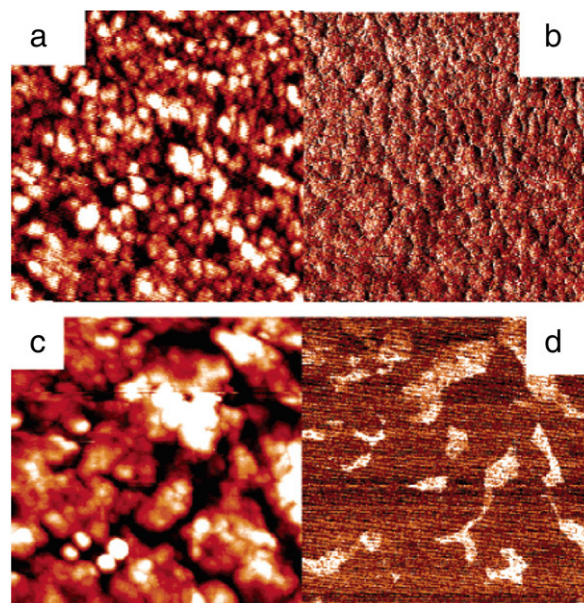

Fig. 12. Simultaneous STM (left) and BEEM (right) images of an nTP-Au/octanedithiol/n-GaAs diode (c, d) compared with a reference Au/n-GaAs diode (a, b). The images are obtained at $I_{tip} = 20$ nA and at $V_{tip} = -1.8$ V and -2.1 V, respectively. The scan area is 200×200 nm². The contrast range in the STM images is 5.4 nm and 20 nm for (a) and (c), respectively. The contrast range in the BEEM images is 300 ± 50 pA and 5 pA for (b) and (d), respectively. Reprinted with permission from Ref. [89].
© 2005, American Chemical Society.

possible damage of the molecular layer during the conventional evaporation process, an "nTP" process is used to make the Au base contact. In this process, a Au coated poly(dimethylsilozane) stamp is used to transfer the contacts to the molecular layer. The presence of the C8DT molecular layer was found to drastically increase the BEEM threshold voltage from −0.9 V to −1.4 V as well as to drastically decrease the overall interface transparency (Figs. 12 and 13). Interestingly, the BEEM current starts to drop for tip biases above −2 V, indicating that the BK model, developed for m–s interfaces, cannot be directly applied. A simple model of the molecular layer as a tunnel barrier of 5 eV with an extra molecular state could reproduce the decrease of BEEM current at high biases. This suggests that the BEEM threshold increase is due to the unoccupied molecular level rather than a change in the m–s band alignment.

In hybrid systems with a discontinuous monolayer of polar molecules at the m–s interface, the dipole field of the molecular layer perpendicular to the surface may affect electron transport through the m–s interface near the embedded pinholes. This is supported by a systematic BEEM study of a discontinuous monolayer of dicarboxylic acid (dC-X) sandwiched between Au and n-GaAs. In this system the dC-X forms an electric dipole layer at the GaAs interface with a perpendicular dipole moment depending on the functional end group "X" (= OCH_3, CN, and CF_3) [90].

For most of the area covered by the molecular monolayer, the BEEM current was found to be very small and the threshold voltage was found to increase to −1.4 V (Fig. 14). The apparent barrier height of 1.4 eV was not fully understood, and was tentatively attributed to photon emission in the metal base as well as electron–hole pair generation in the GaAs substrate [91]. At pinholes where the BEEM current was larger, a lower threshold of −0.95 V was found. The local apparent barrier heights at the pinholes are believed to be modified by the dipole field of surrounding molecules, a proposal supported by electrostatic modeling [92]. This value is consistent with macroscopic *I–V*, *C–V* and
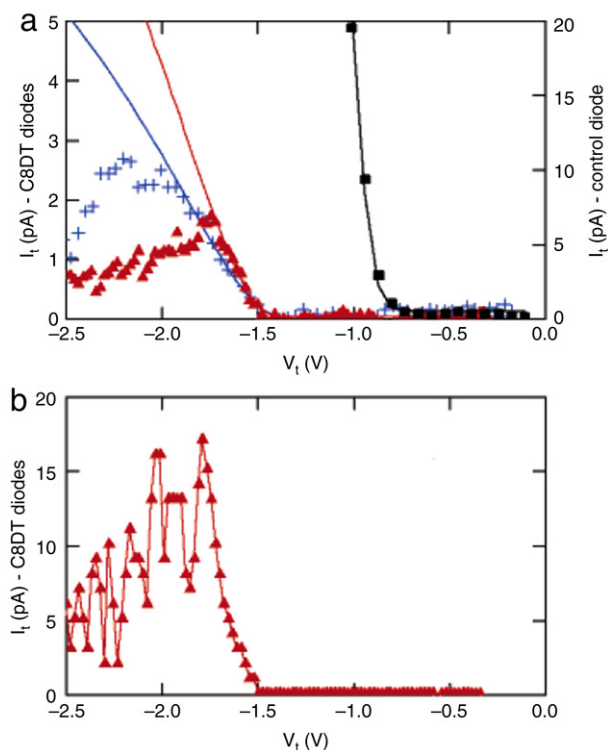
Fig. 13. (a) Average of 10 BEEM spectra measured at random spots in the high transmission regions in the nTP-Au/octanedithiol/n-GaAs diode of Fig. 12(d) (triangles) compared to that of an evaporated-Au/octanedithiol/n-GaAs diode (crosses) and a control Au/n-GaAs diode (squares) obtained at $I_{tip} = 20$ nA. The solid lines are fits by the Bell–Kaiser model. (b) A relatively strong single BEEM spectrum from the same nTP-Au/octanedithiol/n-GaAs diode. Reprinted with permission from Ref. [89].

IPE measurements, indicating that such measurements are dominated by leakage current through pinholes in molecular monolayer. Another study on Au/titanylphthalocyanine(TiOPc)/GaAs diodes also found an increase in the Schottky barrier height, which showed an approximately linear increase from 1.2 eV at room temperature to 1.5 eV at 10 K [93].

Although several BEEM experiments are reported on buried organic molecules, only one theoretical work on such systems has been published so far. Kirczenow studied ballistic transmission of electrons through alkanes (C_nH_{2n+1}) and alkanethiol ($C_nH_{2n}S$) molecules of moderate length chemisorbed on a silicon substrate and buried under a thin Au film using a semiempirical tight-binding model [94]. This model is based on an "extended molecule" that includes the molecule itself as well as clusters of metal atoms forming the electric contacts, which follows the same scheme used for transport simulations in molecular electronics. The Au STM tip is represented by a cluster of 10 Au atoms in a (111) geometry, terminating with a single atom. The Au film between the tip and molecule is represented by a cylindrical cluster of 591 Au atoms with (111)-oriented facets to the STM tip and the molecule. The Si substrate is represented by a hemispherical crystallite of 390 Si atoms with the dangling Si bonds passivated by H atoms and its flat (111) surface facing the molecule (see Fig. 15).

One of the main conclusions of this work is that if the molecules are formed by saturated C–C bonds at a moderate molecular length, e.g. decane ($C_{10}H_{21}$), decanethiolate ($C_{10}H_{20}S$) and hexanethiolate ($C_6H_{12}S$), the insulating nature of these molecules results in a transmission probability so weak that the collector current ratio I_C/I_{tip} is much lower than the nominal sensitivity threshold for practical BEEM experiment, 10^{-5}. On the other hand, resonant transmissions through molecular states in semiconducting molecules with unsaturated C–C bonds or aromatic rings are predicted to be strong enough to be resolved in BEEM current (see Fig. 15).

3.2. BEEM of adsorbate organic molecules

Currently, there are several issues associated with applying BEEM to buried organics. The chemical stability and mechanical strength of semiconducting organic molecules are in general inferior to that of their inorganic counterparts. The coating methods for organic thin films and metal overlayers are delicate processes [89] and often introduce local variations and defects that may disturb the measured BEEM current. The diode characteristics in ambient environments degrade over time [89]. It is often observed that acquisition of BEEM spectra at the same spot accelerates the diode degradation, similar to the case of MIS structures. Finally, the granular polycrystalline Au overlayer used so far as the base contact inevitably reduces the BEEM spatial resolution, especially if imaging of a single buried molecule is desired.

To circumvent the above problems, adsorbates can be placed on top of the metal base film instead of burying the organic molecules under the metal overlayers. The metal base film is preferably epitaxially grown on the semiconductor substrate [95,96]. This is beneficial for BEEM studies of single molecules because of the improved collector transfer ratio and a more homogeneous BEEM contrast compared with the case of polycrystalline base films.

These ideas were recently demonstrated by a UHV STM/BEEM study of the fullerene C_{60} and planar organic molecule PTCDA (3, 4, 9, 10-perylene-tetracarboxylic acid dianhydride) deposited on atomically flat surfaces of bismuth (Bi) monolayers on silicon [97].

Since the Schottky contact between the Bi and Si(100) is prepared homogeneously, the BEEM current transmitted through the molecular adsorbates is mediated by the specific molecular electronic states at the injection energy. Indeed, BEEM current measured on a single C_{60} molecule reveals a second voltage threshold at 1.48 eV (see Fig. 16). This is consistent with the energy level of the first excited unoccupied electronic state (LUMO + 1) measured by two-terminal STM spectroscopy. BEEM images show relatively higher transmission through the perimeters of C_{60} molecules, providing the first spatial image of molecular orbitals (see Fig. 17). Similar results were obtained on PTCDA molecules. These exciting results demonstrate that a combined STM/BEEM study is capable of unveiling sub-molecularly resolved electronic properties of organic molecules in great detail.

4. Hot-electron luminescence

A question that has remained largely unaddressed so far in the field of BEEM is whether or not one can obtain information on local carrier transport and luminescent properties simultaneously. If it were possible, such a tool would be especially useful to unveil light emission properties of emerging inorganic and organic semiconducting nanostructures such as epitaxially-grown self-assembled quantum dots (QDs), synthetic inorganic nanocrystals and organic molecules. These structures hold great promise in optoelectronics but are difficult to characterize due to their small dimensions.

It is well established that a semiconductor laser that uses QDs with three-dimensional electron–hole confinement in the active gain medium is superior in many aspects to traditional quantum well (QW) lasers with one-dimensional confinement in the active medium [98]. This is owed to the beneficial effects of discrete atomic-like DOS on the optical properties. For optoelectronic
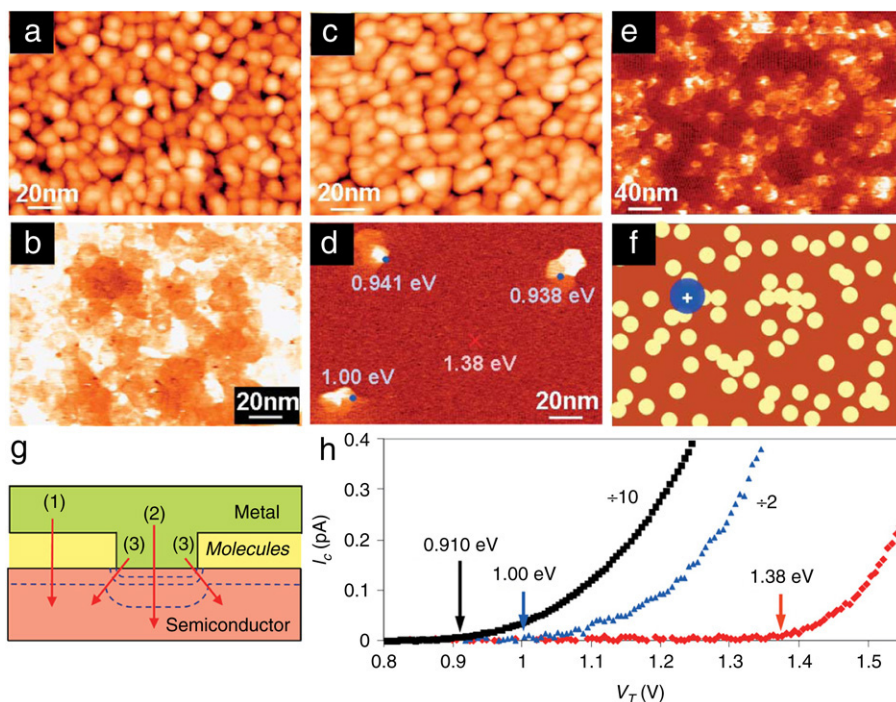
Fig. 14. Simultaneous STM (a) and BEEM (b) images of a control Au/GaAs sample with $V_{tip} = -1.2$ V (gray scales: (a) 3.4 nm and (b) 3 pA), compared with STM (c) and BEEM (d) images of a Au/dC-CH$_3$/GaAs sample with $V_{tip} = -1.4$ V (gray scales: (c) 3.6 nm and (d) 1 pA), and BEEM image (e) of Au/dC-OCH$_3$/GaAs sample with $V_{tip} = -1.4$ V (gray scale: 4 pA). The origin of "pinholes" in BEEM image of (d) is illustrated in (f). All images are measured at $I_{tip} = 20$ nA. (g) Illustration of the equipotential profile (dashed lines) and electric field (arrows) near a pinhole in a molecular layer. (h) BEEM spectra and measured Schottky barrier height from: Au/GaAs (squares), pinhole in lower-left of image (d) on Au/dC-CH$_3$/GaAs sample (triangles) and non-pinhole regions of dC-CH$_3$ sample (diamonds). Reprinted with permission from Ref. [90].
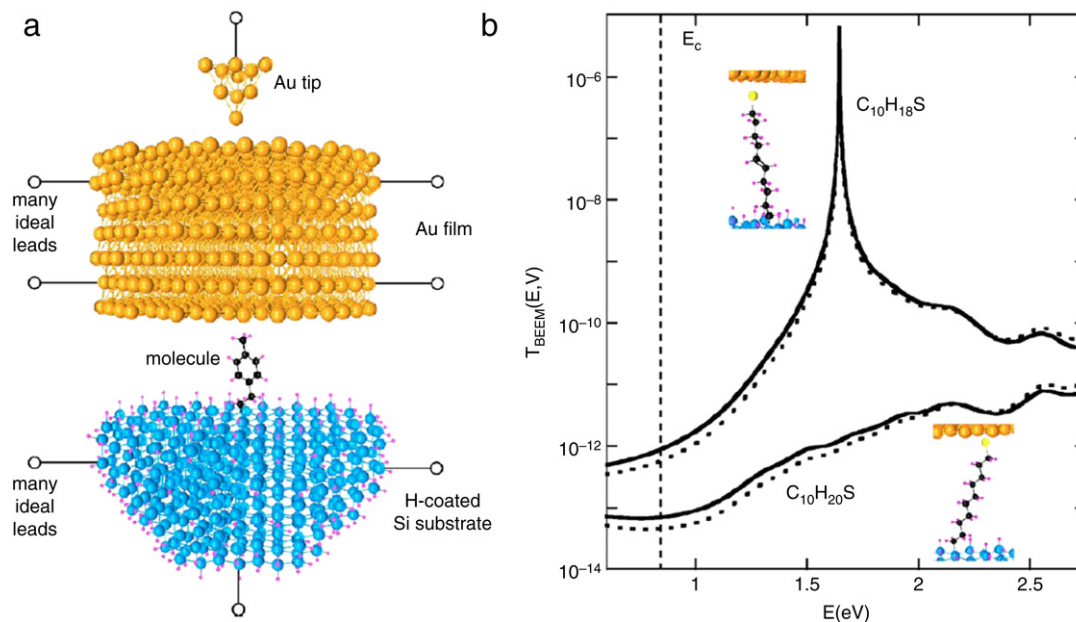© 2006, Wiley-VCH.

Fig. 15. (a) The "extended molecule" used to model BEEM transport through an organic molecule (e.g. ethylmethylbenzene) chemisorbed on a silicon substrate and buried under a thin Au film. (b) Calculated electron transmission probabilities $T_{BEEM}(E, V)$ from a STM tip through a gold film, molecule and silicon substrate. Molecules with saturated C–C bond (e.g. decanethiolate C$_{10}$H$_{20}$S) show very low T_{BEEM}. A resonant transmission is seen for the C$_{10}$H$_{18}$S molecule due to the presence of a double C–C bond. Reprinted with permission from Ref. [94].
© 2007, American Physical Society.

applications, QDs must be highly uniform in size and shape as well as free of defects and impurities. The introduction of a local probe technique to examine the carrier transport and photon emission in buried optically active QD layers will provide a means to study the correlations between QD growth parameters and their properties

such as size and shape, defect densities and charge carrier capture and recombination mechanisms. This knowledge would facilitate the advancement of the QD laser.

Unfortunately, such a technique is generally not available. The fact that the electron–hole recombination occurs in buried active
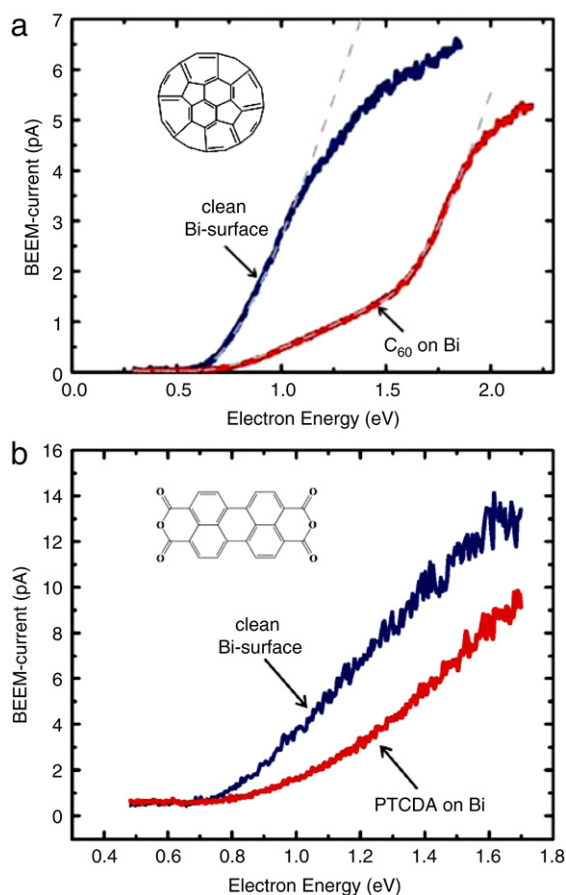
Fig. 16. (a) BEEM spectra measured on clean Bi/Si(100) and on a single monolayer of C_{60} absorbed on the surface of Bi. A Schottky barrier height of $\phi_S = 0.58$ eV is obtained by an empirical power-law fit to $(eV_{tip} - \phi_S)^2/eV_{tip}$ (dashed line). The resonance through the LUMO + 1 level of C_{60} is seen at 1.48 eV. (b) BEEM spectra measured on clean Bi/Si(100) and on a single monolayer of PTCDA absorbed on Bi. Insets show the molecular structures of C_{60} (top) and PTCDA (bottom). Reprinted with permission from Ref. [97].
© 2007, AAAS.

layers is a main hurdle which obscures these processes from direct observation. Micro-photoluminescence (μ-PL) [99] and near-field scanning optical microscopy (NSOM) [100] are, in principle, capable of single QD characterization. However, the optically-pumped excitation process involved is fundamentally different from carrier injection in realistic light-emitting devices. Cathodoluminescence (CL) from a scanning electron microscope has a high resolution due to a focused electron beam, but the kinetic energy of injected electrons (10^2–10^3 eV) is much higher than the case of electrical pumping (1–10 eV). For these reasons, exploration of a new luminescent scanning probe method is of considerable interest. Here, a brief retrospective review of two-terminal hot-electron luminescence is presented first, then the development of a three-terminal hot-electron luminescence technique is introduced.

4.1. STM luminescence

The first local photon emission phenomenon in STM was observed in 1988 [101]. It was soon developed into a technique, scanning tunneling luminescence (STL) microscopy, by recording the luminescence intensity and topographic image simultaneously to produce a spatial image of the photon emission [102,103]. As a two-terminal hot-electron luminescence technique, STL has been generally used to study two categories of structures, metal–metal and metal–semiconductor tunnel junctions.
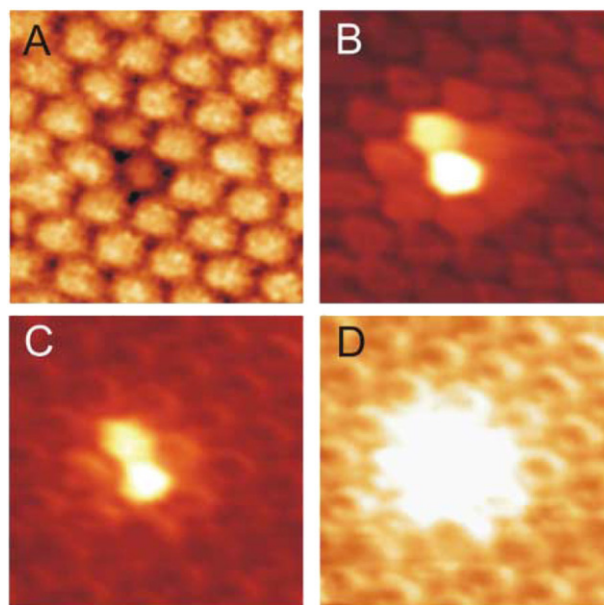

Fig. 17. Simultaneous STM (A) and BEEM (B) images of a C_{60} monolayer island on Bi/Si at $V_{tip} = -1.3$ V and $I_{tip} = 40$ pA. Scan area is about 5×5 nm. Gray scales are 0.2 nm (A) and 0.2–4 pA (B), respectively. (C) and (D) are BEEM images at $V_{tip} = -2.1$ V with scales of 0.2–4 pA and 0.2–1 pA (to enhance the contrast), respectively. Reprinted with permission from Ref. [97].
© 2007, AAAS.

4.1.1. Metal–metal junctions

In the case of a metal/vacuum/metal tunnel junction, the primary physical processes involved are inelastic tunneling due to surface plasmon (SP) excitation and de-excitation [104]. Surface plasmons are surface electromagnetic waves that propagate along a metal/dielectric (or metal/vacuum) interface. Surface plasmon modes existing in a STM tunnel junction can be excited by the energy loss of inelastically tunneling electrons. Although SP modes are nonradiative in nature due to their dispersion relationships, they can be coupled into a radiation mode by scattering processes, provided the momentum matching condition is satisfied.

4.1.2. Metal–semiconductor junctions

In the case of a metal/vacuum/semiconductor tunnel junction, photon emission belongs to a category of phenomena called inverse photoemission [105]. Because of its technical importance, only band-to-band luminescence in a semiconductor substrate induced by tunnel electrons will be considered. Band-to-band luminescence can be induced by injecting either minority carriers or majority carriers. Fig. 18 shows the case of electron injection into a p-type semiconductor by a negatively biased STM tip (minority carrier injection) [102]. Fermi level pinning at the surface due to surface states produces a downward band bending which pushes holes out of the depletion region near the surface. To be able to recombine with holes in the bulk, tunnel injected electrons have to ballistically traverse the depletion region. This is only possible if the applied tip bias is higher than the bandgap energy (the energy difference between the conduction bandedge and the Fermi level in the bulk) as required by the law of energy conservation in a linear system. It was found that the luminescence intensity follows a quadratic response with the applied voltage near the threshold regime [103]. This can be justified by theoretical arguments similar to the case of BEEM or IPE.

For electron injection into an n-type semiconductor by a negatively biased STM tip (majority carrier injection), injecting hot electrons with kinetic energies much greater than the bandgap
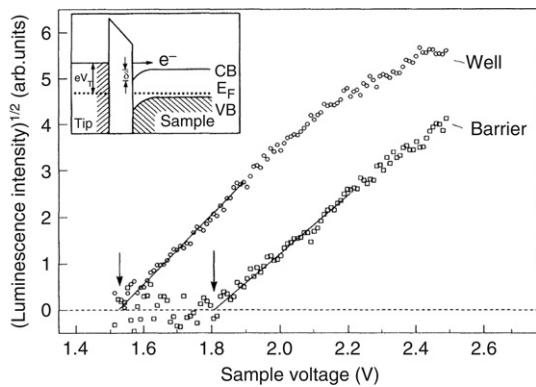
Fig. 18. Luminescence intensity vs voltage spectra produced by minority carrier injection into an $Al_{0.1}Ga_{0.9}As/Al_{0.3}Ga_{0.7}As$ heterostructure. The inset shows the schematic energy diagram. Reprinted with permission from Ref. [103]. © 1991, American Physical Society.

can induce impact ionization and excite electron–hole pairs across the bandgap. The electron–hole pairs then recombine radiatively into photons, a mechanism similar to avalanche multiplication in semiconductor diodes under high reverse bias.

It is worth noting that whether majority or minority carriers are injected, band-to-band luminescence occurs only if the tunnel voltage bias is larger than the bandgap energy. This conclusion can be simply drawn from the energy conservation perspective, except for nonlinear processes such as the generation of one photon by two electrons.

4.1.3. Heterojunction devices

As a related method, ballistic electron luminescence spectroscopy (BELS) has been used to study hot-electron luminescence in heterojunction-based solid-state devices [106,107]. Conceptually, it is similar to STL in the case of minority injection. By applying a voltage bias higher than the bandgap energy, hot electrons are tunnel injected via heterojunctions into a p-type GaAs. Once inside the GaAs they travel ballistically until radiatively recombining with neutral acceptors at low temperatures. Thermalization of ballistic electrons by longitudinal optical (LO) phonon emissions was manifested by multiple electroluminescence peaks separated with LO phonon energy ($\approx$37 meV in GaAs) (Fig. 19). This technique was used to study ballistic electron transport in GaAs including LO-phonon scattering and electron attenuation lengths.

4.2. BEEM luminescence

4.2.1. Bipolar collector

Since STL is not able to probe sub-bandgap energy barriers, it is of particular interest if electroluminescence can be produced in a three-terminal BEEM setup. A technique which is generally capable of measuring sub-bandgap energy barriers. Early efforts to produce light emission using minority carrier injection in a typical BEEM configuration (with collector unbiased) turned out to be futile. One notable exception is weak light emission from SP modes in a Au base film [108]. This can be understood again from the energy conservation perspective. The fast hot-electron thermalization process inside the semiconductor collector posts an upper limit of the extra kinetic energy gained from ballistic injection as the Schottky barrier height, which is typically smaller than the optical transition energy. Applying an additional voltage bias across the collector can, in principle, make up the energy discrepancy between band-to-band luminescence and the Schottky barrier height.

This design principle was first confirmed in 2003 by Russell et al. in an internal photoemission luminescence (IPEL) device [109].

This device works as a linear photon up-converter that absorbs sub-bandgap photons with energy higher than the Au/GaAs Schottky barrier height ($\sim$0.9 eV) but less than the bandgap energy of GaAs (1.42 eV), and generates GaAs bandedge luminescence with a forward collector bias $V_C > 0.7$ eV (see Fig. 20). It was found that the sum of V_C and the excitation photon energy needs to be $\sim$0.2 eV greater than the GaAs bandgap to induce GaAs emission. The extra energy loss of $\sim$0.2 eV is due to the hot-electron relaxation inside the semiconductor collector.

Replacing IPE excitation with tunnel emission excitation, Appelbaum et al. used the same heterostructure to demonstrate a three-terminal hot-electron luminescence device in order to perform ballistic electron emission luminescence (BEEL) (see Fig. 21) [110]. As a proof-of-concept, a solid-state $Al/AlO_x/Al$ tunnel junction was used instead of a STM setup to improve the signal-to-noise ratio. The collector heterostructure was similar to an asymmetric pn-junction diode with the GaAs QW recombination region cladded between a heavily p-doped AlGaAs bottom layer and a lightly n-doped (n $\sim 10^{17}$ cm^{-3}) AlGaAs top layer (see inset of Fig. 20(b)). Such a band profile forms a valence-band potential barrier to suppress the overwhelming majority carrier (hole) current under a forward collector bias. Cryogenic temperatures ($<$150 K) were used to further suppress the thermionic majority current. GaAs emission was observed under the condition that $V_{EB} > \phi_S$ and V_C was larger than the energy discrepancy between the GaAs emission energy and ϕ_S. Such a scheme can, in principle, be used to simultaneously obtain interfacial carrier filtration and light emission properties of photonic materials. Room-temperature STM-based BEEL operation was also demonstrated, although BEEM spectra could not be measured due to the overwhelming internal majority current [111].

Using a cryogenic STM/BEEM setup, Yi et al. demonstrated a combined BEEM/BEEL spectroscopy of a heterostructure device with a layer of self-assembled InAs QDs as the optically active region [112]. Because of their much higher collector current injection levels, planar tunneling devices were also used to acquire the wavelength spectroscopy of the QD luminescence. These measurements resolve QD ground-state emission near 1.34 eV (confirmed with a V_C-dependent Stark shift), and GaAs emission at 1.48 eV (see Fig. 22(c)). In the case of STM, luminescence intensity was measured in a far-field configuration by an avalanche single-photon counter coupled through a multimode optic fiber to the tunnel position. A good match was found between the overall V_C dependence of spectrally-integrated luminescence intensity measured from the planar tunneling device and luminescence intensity measured from STM. The latter showed a large inhomogeneity over different tip locations and extra features possibly related to luminescence from excited states of the same QD or QDs with different sizes [113]. By suppressing the internal majority current at low temperatures, consistent BEEM current spectra were acquired with both STM and planar devices (see Figs. 21 and 22(a) and (b)).

4.2.2. Fundamental and technical challenges

4.2.2.1. Spatial resolution. The ballistic nature of hot-electron transport in BEEM experiments is only valid under certain conditions. As already discussed in the previous BEEM review [6], the depth resolution of BEEM for buried heterostructures is restricted by the mean free path (mfp) inside the semiconductor. For well-characterized GaAs material, Monte Carlo simulations of electron transport in the Γ, L, and X valleys found strong energy-dependent mfps limited by electron–phonon scattering and intervalley scattering [114–116]. At $T = 300$ K, the mfp for the Γ, L, and X valleys near their energy thresholds are $\sim$100, $\sim$10, and $\sim$1 nm, respectively. Cooling the sample to lower
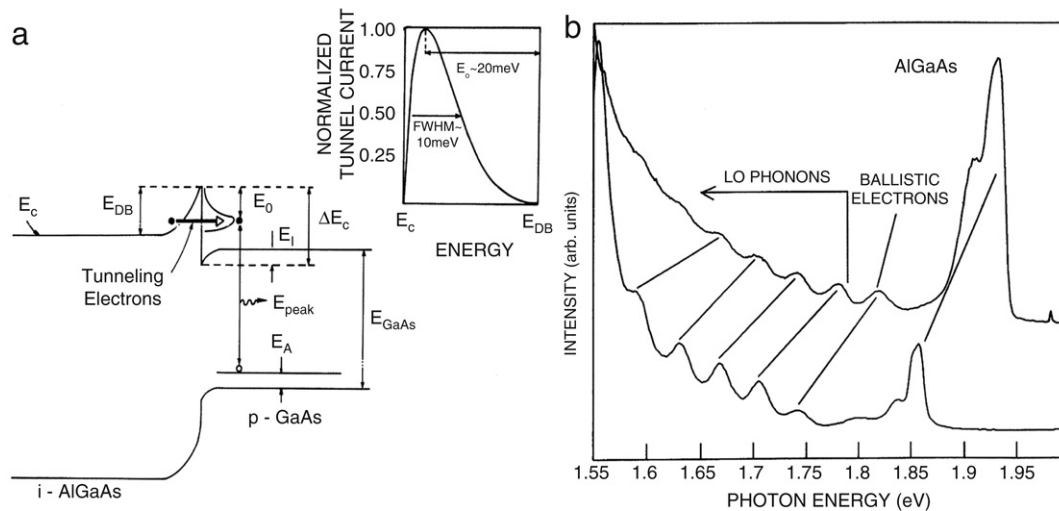
Fig. 19. (a) Schematic band diagram of a BELS device (not to scale). If the diode is forward biased at low temperatures, hot electrons are tunnel-injected into the p-GaAs and recombine with neutral acceptors. LO-phonon emissions may occur before the recombination happens. (b) Electroluminescence spectra from the same BELS device in (a) (upper curve) and a device with the p-GaAs separated from the heterojunction with a 100 nm undoped GaAs spacer layer (bottom curve). Both are taken at 6.5 K. Reprinted with permission from Ref. [107].
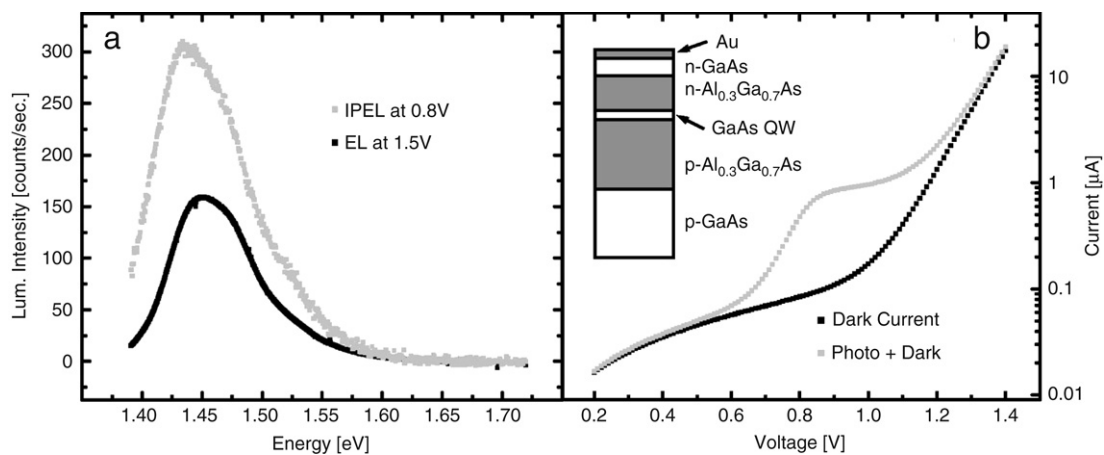© 1992, Institute of Physics.

Fig. 20. (a) Electroluminescence and IPEL spectra of an IPEL device. (b) Current–voltage characteristics of the same device which shows a substantial photocurrent for biases larger than ∼0.7 V with a monochromatic sub-bandgap photoexcitation ($\lambda = 980$ nm). The inset is a schematic of device structure. Reprinted with permission from Ref. [109].
© 2003, American Institute of Physics.

temperatures does improve the mfp due to the change in phonon populations. At 85 K, the overall scattering rates decrease by a factor of ∼2. As a result, the calculated mfp for the Γ and L valleys increases from ∼100 to ∼150 nm, and from ∼10 to ∼30 nm, respectively. The mfp for the X electron is too short to be considered in BEEM heterostructures. The increased mfp for L valley electrons is supported by experimental BEEM results on Au/GaAs/AlGaAs single-barrier samples at $T = 85$ and 300 K [16]. Monte Carlo simulations have found significant electron cooling (∼3 meV/nm at $V_{tip} = 1.5$ V) due to phonon emission at electron energies higher than 0.65 eV above the Γ valley minimum. These same simulations also show significant redistributions of electron populations among the conduction band valleys. With increasing depth, the relative population of the Γ valley increases (see Fig. 5 in Ref. [116]).

As a result, for GaAs-based structures, the mfp of the Γ electrons determines the depth resolution of BEEM. The same situation applies to BEEL heterostructures. The GaAs QW in the first BEEL device is buried at a depth of 120 nm below the m–s

interface [110], which is still within the mfp of the Γ valley electrons at ∼77 K. However, the spatial resolution is expected to be deteriorated due to broadening of electron distribution. Room temperature Monte Carlo simulations showed that 30 nm wide quantum wires will show significant BEEM contrast at a depth of 60 nm due to the added dimension, while 30 nm diameter quantum dots are hardly detectable. Reducing the depth of the optically active layer will improve the spatial resolution for BEEL imaging, however, this is limited by the fact that the optically active layer cannot be fully depleted by the Schottky contact, making majority carriers unavailable for radiative recombination.

4.2.2.2. Nonradiative recombinations. Since a BEEL device operates at low current injection levels, nonradiative recombination pathways can be serious competitors of radiative recombination. The three major electron–hole recombination mechanisms in direct-gap semiconductors are radiative band-to-band spontaneous recombination, nonradiative Shockley–Hall–Read (SHR) and Auger
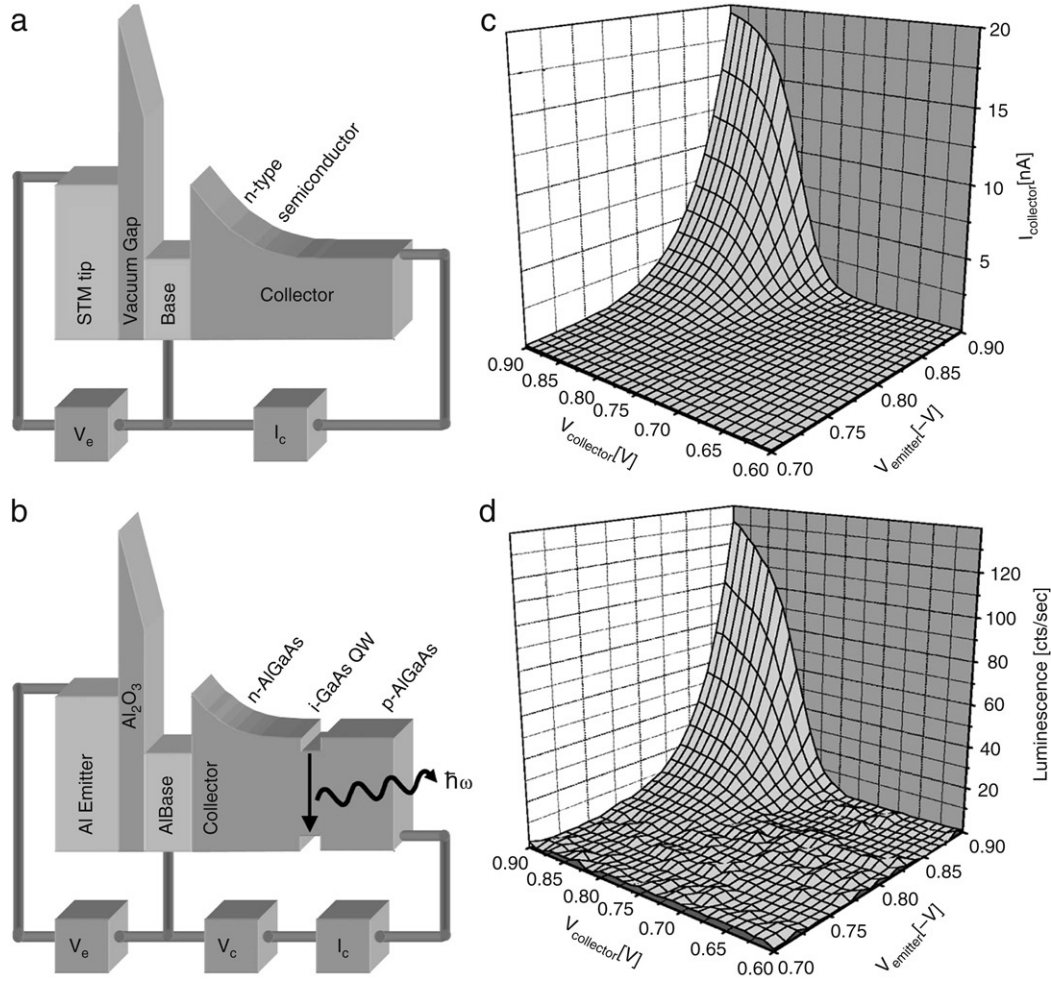
Fig. 21. Schematic energy band diagrams of a STM/BEEM setup (a) compared with a planar tunneling BEEL device (b). (c) Collector current spectroscopy for a BEEL device. (d) Luminescence intensity for the same device. Reprinted with permission from Ref. [110].
© 2003, American Institute of Physics.

recombinations. These three recombination rates can be expressed as:

$$R_{bb} = B(np - n_i^2) \tag{12}$$

$$R_{SHR} = \frac{np - n_i^2}{(p + n_i)\tau_n + (n + n_i)\tau_p} \tag{13}$$

$$R_{Auger} = A_n n^2 p + A_p p^2 n. \tag{14}$$

Here n, p, and n_i are electron, hole, and intrinsic carrier concentrations. τ_n and τ_p are electron and hole minority carrier lifetimes. B is spontaneous recombination coefficient. A_n and A_p are electron and hole Auger recombination coefficients. In Eq. (13), mid-gap SHR recombination centers are assumed for simplicity. The three recombination rates inside a GaAs quantum well in a BEEL device are calculated as a function of collector bias using a one-dimensional device simulator based on drift-diffusion model in Fig. 23 [117]. Since the device operates at a low minority carrier (electron) injection level inside the quantum well ($n_i \ll n \ll p$), it can be easily deduced from Eqs. (12)–(14) that all three recombination rates are approximately proportional to the electron concentration n. Therefore they have similar voltage dependence, differing only in magnitude. As would be expected for low level injection, the effect of Auger recombination is negligible. However, the nonradiative SHR recombination rate is on the same order of magnitude as spontaneous recombination rate. This is undesirable for the BEEL device operation. Cooling the device

to lower temperatures may help to suppress nonradiative SHR recombination by reducing the capture cross sections for minority carriers.

4.2.2.3. Photon collection. Although the concept of BEEL was demonstrated in spectroscopic measurements, there are still significant challenges towards implementing it in microscopic mode. One of the major technical challenges is to measure the very weak photon signals generated by a ∼pA collector current. Taking into account competitive nonradiative recombination pathways and the collection efficiency of far-field optics, the overall power efficiency of a BEEL device is extremely small. Recently, it was found that this difficulty could be overcome by directly integrating a photodetector onto the same heterojunction collector (see Fig. 24) [118,119]. This solved the refractive index mismatch issue and drastically improves the collection efficiency by reducing the distance and increasing the collection solid angle. A photocurrent approximately 10% of the BEEM current was measured, indicating that at least one photon is generated per 10 electrons injected. This increase in detection sensitivity was obtained at the expense of wavelength sensitivity.

4.2.3. Unipolar collector

The use of a bipolar (pn-junction) collector doping profile in BEEL introduces a quadratic band bending and non-constant electric field. This is not optimized for BEEM measurement of subsurface potential barriers. To solve this problem, a unipolar
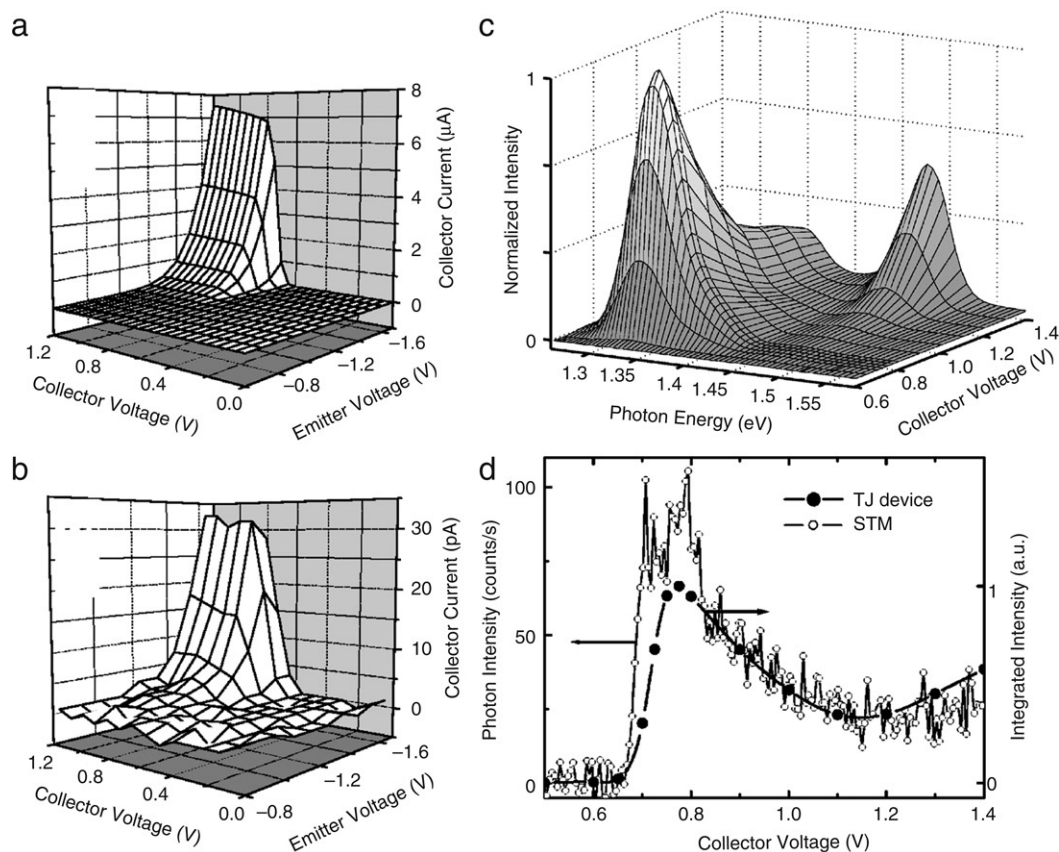
Fig. 22. Typical BEEM spectra for a three-terminal hot-electron luminescence device with the emitter consisting of a planar Al/AlO$_x$/Al tunnel junction (a) and a STM tip (b). STM spectra was taken at I_{tip} = 4 nA. Wavelength-resolved luminescence spectra measured with a planar tunneling device (c). V_C dependence of the spectrally-integrated luminescence intensity from the planar tunneling device compared to a luminescence spectrum obtained with STM tip injection (d). Reprinted with permission from Ref. [112].
© 2004, American Institute of Physics.

collector heterostructure was designed, with the recombination region (a layer of self-assembled InAs QDs) embedded in undoped cladding layers grown on a p-type substrate (see Fig. 25) [120]. Such a design gives rise to a linear band profile and hence a constant electric field in the undoped layers. The electric field can be adjusted by a collector bias to reach a nonequilibrium flat-band condition, accommodating BEEM measurements of buried barrier heights. A GaAs/Al$_{0.4}$Ga$_{0.6}$As short-period superlattice blocking layer was used to reduce the internal majority (hole) current under forward collector bias. This ensured that the ballistically injected electron current was measured. The base–collector structure mimics an FET, making it also suitable for optical studies such as μ-PL and absorption spectroscopy.

Depending on the direction of the electric field inside the collector, majority (holes) or minority (electrons) carriers are injected by either the reverse mode or direct mode of BEEM. This makes it possible to measure the maximum barrier height (formed by the Al$_{0.4}$Ga$_{0.6}$As layer) in the valence and conduction band on the same sample, and consequently the bandgap of Al$_{0.4}$Ga$_{0.6}$As. Compared with traditional BEEM using an unbiased collector, this method of subsurface bandgap measurement utilizing ambipolar carrier injection has an advantage that experimental errors due to possibly different Fermi level pinnings in p-type and n-type specimens can be avoided.

5. Cross-sectional BEEM

Since 1986, cross-sectional STM (x-STM) has been used to study various epitaxial semiconductor structures [121]. In this
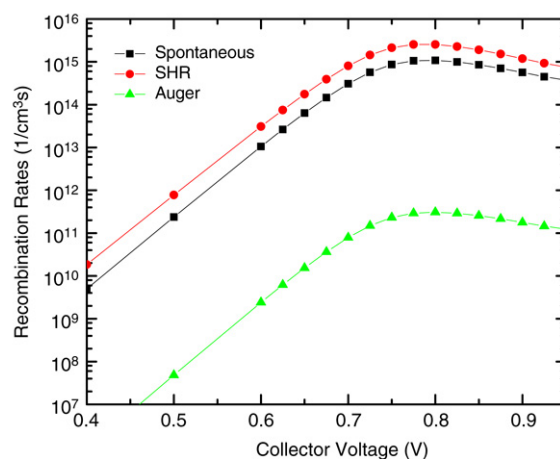

Fig. 23. Collector bias dependence of the simulated room temperature recombination rates inside a GaAs quantum well of the BEEL device in Ref. [110]. Reprinted with permission from Ref. [113].

method, a cross section of the single crystal structure is prepared by *in situ* cleavage in a UHV STM. This is especially suited to studying layered heterostructures, since it gains information on the interfaces between layers as well as on the individual layers themselves. Because of their relative ease of cleavage, most of the x-STM studies are performed on III–V semiconductors. For GaAs, the (110) cleavage surface has an additional benefit that the surface states lies outside the bandgap
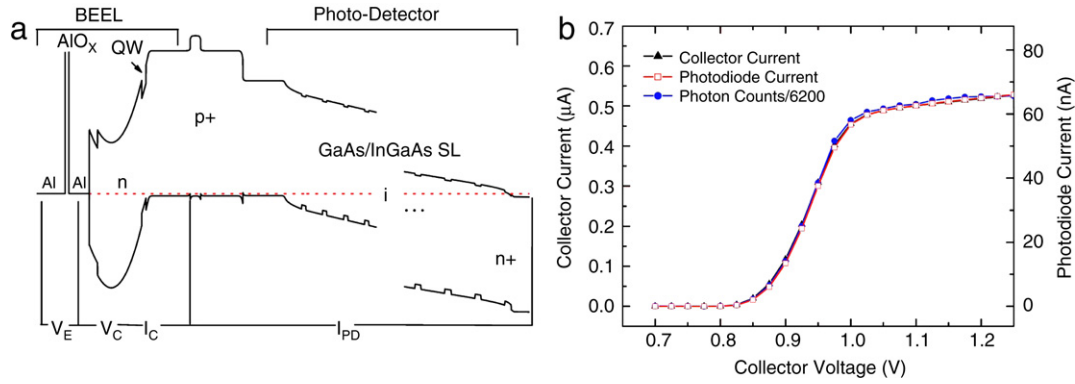
Fig. 24. (a) Energy band diagram of a vertically-integrated device with a BEEL region (left) and integrated photodiode (right). Shown are the emitter bias (V_E) collector bias (V_C), collector current (I_C) and photocurrent (I_{PD}). (b) Comparison of the collector bias dependence of the collector current (closed triangles), on-device photodiode current (open squares) and externally collected luminescence (closed circles) at a constant emitter bias of −1.4 V at 77 K. Reprinted with permission from Ref. [119]. © 2006, American Institute of Physics.
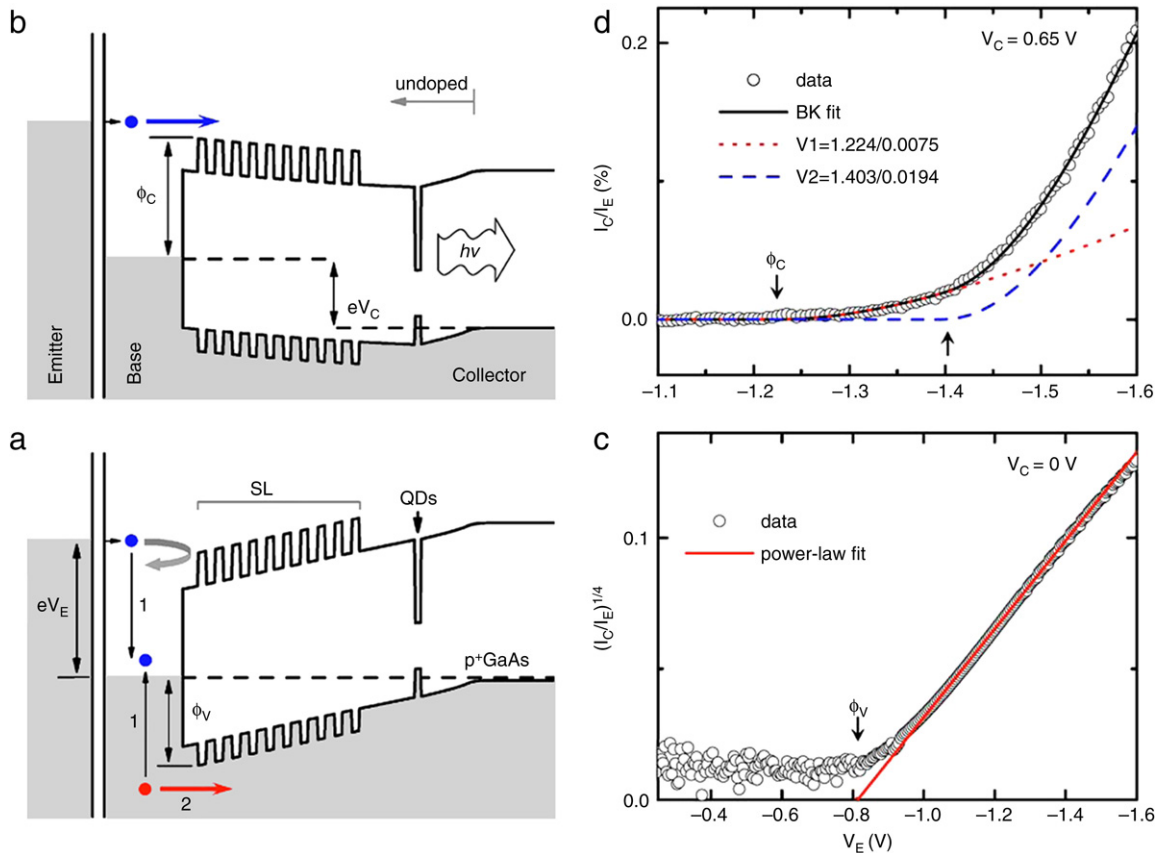

Fig. 25. Schematic band diagrams of a BEEL device with a unipolar p-type collector illustrating majority carrier (hole) injection with an unbiased collector ($V_C = 0$ V) (a), and minority carrier (electron) injection with the collector under forward bias ($V_C > 0$ V) (b). A negative emitter bias, V_E is used to inject hot electrons into the base. The corresponding BEEM spectra at $V_C = 0$ V and $V_C = 0.65$ V are plotted in (c) and (d), respectively. Reprinted with permission from Ref. [120]. © 2007, American Physical Society.

so that bulk properties of the bandgap, band offsets and other features can be investigated through spectroscopic studies. Only a few experiments have been reported on group IV materials [122–124].

Cross-sectional BEEM (x-BEEM) has only recently been reported by two groups [125–127]. There are several technical challenges performing x-BEEM, including *in situ* fabrication of the Schottky diode and making a nondestructive macroscopic contact to the thin base film. These problems have been circumvented by *ex situ* cleavage of the semiconductor wafer followed by physical evaporation of Au Schottky contacts at pressures of 10^{-7} Torr.

Although *ex situ* processes inevitably introduce an interfacial native oxide layer, it is argued to have minimal effect on BEEM measurements. Furthermore, Schottky barrier heights measured using this type of preparation are more uniform than those samples prepared *in situ* [128].

5.1. Quantum-size effect

Several interesting studies on cleaved GaAs/Al$_{0.3}$Ga$_{0.7}$As quantum wells (QWs) of various width were studied using Au Schottky contacts [125,126]. The measured data was fit to the two-valley BK

model giving Γ and L valley thresholds of 0.9 eV and 1.2 eV for the reference GaAs region and 1.085 eV and 1.21 eV for the $Al_{0.3}Ga_{0.7}As$ barrier layers. The apparent thresholds in the BEEM spectra measured over GaAs QWs were found to systematically increase with decreasing QW width as seen in Fig. 26(a).

BEEM spectra measured over the GaAs QWs were best explained by a linear superposition of a Au/GaAs and $Au/Al_{0.3}Ga_{0.7}As$ spectrum. At a tip bias greater than 1.085 eV some of the hot electrons were injected into the neighboring $Au/Al_{0.3}Ga_{0.7}As$ interface and contributed to the measured BEEM current due to the lateral spreading of the electrons in the Au film. Therefore, the local Schottky barrier height over the GaAs QWs is determined by a single threshold fit of the data at $V_{tip} < 1.085$ eV or a two-threshold fit at $V_{tip} < 1.15$ eV. Both fitting procedures produce similar results within 5 meV. The measured Schottky barrier heights as a function of the QW width d increases systematically with decreasing QW width as shown in Fig. 26(b). Such an increase in the Schottky barrier height is expected due to quantum confinement in the QW conduction band. With the exception of a systematic overestimate, a simple one-dimensional particle-in-a-box model (dashed line in Fig. 26(b)) tracks the measured data fairly well. After including the screening effects of interfacial charge states and image force lowering, the overall estimated Schottky barrier height increase (solid line in Fig. 26(b)) shows very good agreement with the data.

5.2. Lateral resolution

To determine the lateral resolution of x-BEEM, cleaved GaAs/AlGaAs QWs have been used as nanometer-scale apertures of well-defined and controllable width. Analogous to the Rayleigh criterion in optics, BEEM lateral resolution is defined as the minimum separation at which two adjacent QWs could still be resolved in the BEEM current profile. In order to avoid the topography related artifacts from Au grain structures, averaged BEEM current profiles are made over the same GaAs QW. The measured BEEM current profiles show a systematic dependence on the QW width and Au thickness. As shown in Fig. 27(e) and (f), all BEEM current profiles over QWs exhibit a peak with the full-width at half-maximum (FWHM) always significantly larger than the corresponding QW width. The amplitude of these peaks increases with QW width, but is always lower than the amplitude over the wide GaAs region. This is expected since the available unoccupied GaAs conduction band states increases with QW width. The FWHM of these peaks increases while the amplitude decreases with increasing Au film thickness. BEEM lateral resolutions of 12, 16, and 22 nm are found for Au film thicknesses of 4, 7, and 15 nm, respectively. These features are interpreted by significant lateral spreading of hot electrons in the Au film (on the order of 10–20 nm). This is in contrast to the previously suggested "forward-focused" hot-electron distribution (1–2 nm) in the Au film [3]. It is unclear why such a large discrepancy exists. In another study on a similar structure, the broadening of SBH profile across a GaAs/AlGaAs QW was interpreted as a result of lateral band bending effects influenced by single impurities in the AlGaAs layers [127].

6. Advanced insulator films

As CMOS technology proceeds, SiO_2 is no longer a suitable insulating material for metal–oxide–semiconductor field-effect transistors (MOSFET) due to the increase in gate leakage current as the device dimensions shrink. For this reason, SiO_2 is being superseded by insulators with higher dielectric constants, such as HfO_2 and its oxynitrides. There is a high demand for a characterization of these insulators in a MIS structure on the nanoscale. A better understanding of band alignments at the
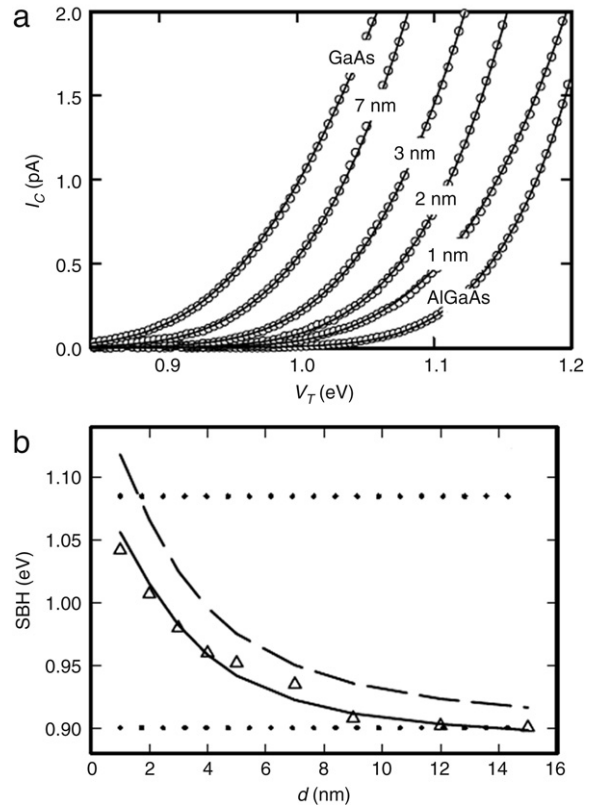

Fig. 26. (a) Measured BEEM spectra (open circles) and the corresponding fits (solid lines) on $Au/Al_{0.3}Ga_{0.7}As$ and a Au/GaAs reference region as well as 7, 3, 2, 1 nm wide GaAs QWs. The data have been scaled for comparison. (b) QW width dependence of the Schottky barrier height (SBH) determined from the experimental data (open triangles) compared with a one-dimensional particle in a box model (dashed line), and the full model (solid line). The dotted lines show the SBH for bulk $Au/Al_{0.3}Ga_{0.7}As$ (top) and Au/GaAs (bottom). Reprinted with permission from Ref. [125].
© 2005, American Physical Society.

insulator/semiconductor interface, hot-carrier transport, bulk and interfacial defects and electric field breakdown mechanisms will aid in optimizing devices utilizing these materials. Compared with traditional characterization techniques such as Fowler–Nordheim tunneling injection and IPE [129–131], BEEM has the advantage of a much higher spatial resolution and the ability to transport electrons across the insulator without using an electric field.

The metal/SiO_2/Si and metal/CaF_2/Si systems are the most well-characterized systems. Detailed results of the insulator conduction band effects such as effective mass and its energy dispersion, charge trapping, MIS device degradation and quantum-size effects, can be found in several review articles [6,86].

BEEM has been used to characterize several high-k dielectric materials as candidates to replace SiO_2 in the CMOS technology. Ludeke studied $W/Al_2O_3/Si$ systems consisting of a 8 nm thick Al_2O_3 layer grown by atomic layer deposition (ALD) on n- and p-type Si substrates ($\rho \sim 1$–17 Ω cm) [86]. The measured conduction band offset between Al_2O_3 and Si was found to be 2.78 eV. BEEM spectra were taken with a broad range of biases V_b applied across the oxide. The BEEM thresholds V_{th} increase for $V_b \leq 0$ as a result of the raising of the oxide barrier, whereas for $V_b \geq 0$ they decrease due to the image force effect. The barrier lowering is given by

$$\delta\phi_S = (qV_{ox}/4\pi\epsilon\epsilon_{if}d_{ox})^{1/2}, \tag{15}$$

where ϵ is the permittivity in vacuum, ϵ_{if} is an image force dielectric constant and d_{ox} is the oxide thickness. The oxide potential V_{ox}
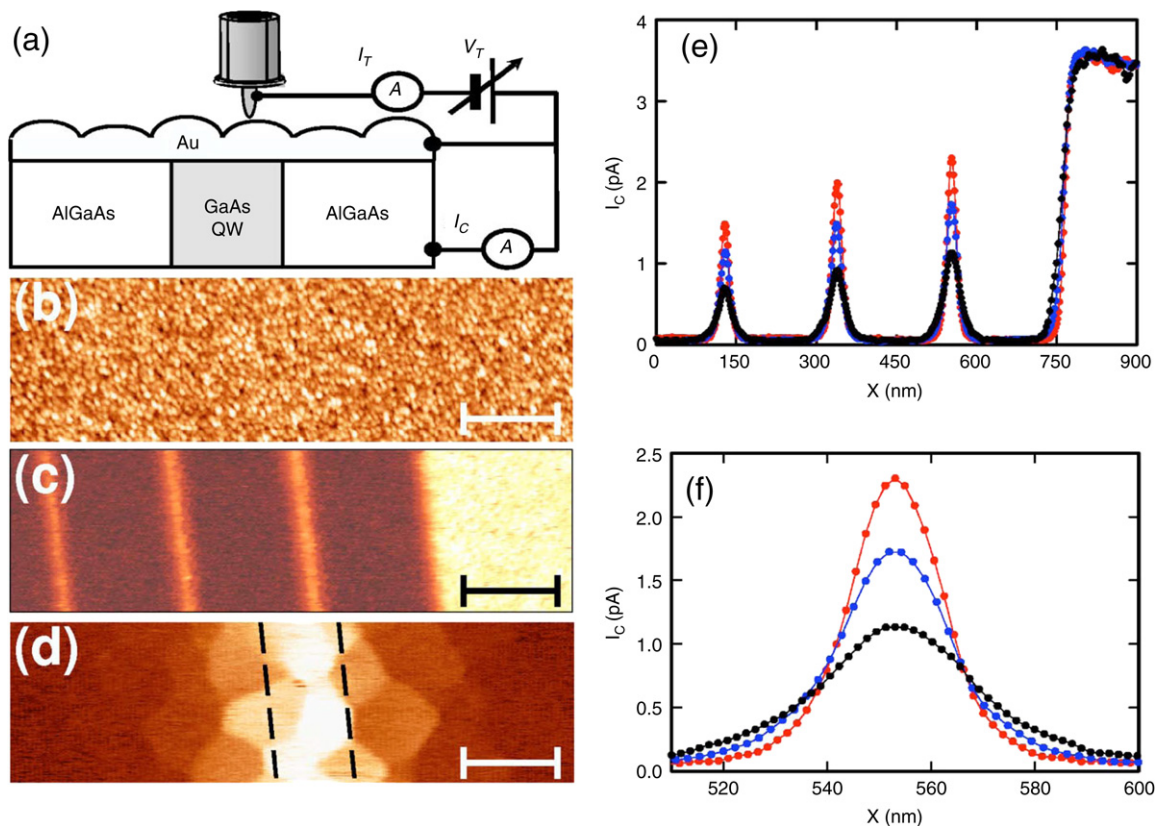
Fig. 27. (a) Schematic of the x-BEEM setup. (b) Simultaneous STM and (c) BEEM images of the same sample region revealing (from left to right) 9, 12, and 15 nm wide GaAs QWs as well as a wide GaAs reference region taken at $V_{tip} = -1.1$ V and $I_{tip} = 15$ nA (scale bar: 150 nm). (d) Zoom-in BEEM image over the 12 nm wide QW that shows the hot-electron spreading effect (scale bar: 15 nm). The dashed line highlights the approximate location of the QW boundaries. (e) Averaged BEEM current profiles over the 9, 12, and 15 nm wide GaAs QWs as well as the wide GaAs reference region for Au film thickness of 4 (red), 7 (blue) and 15 nm (black), respectively. Data acquired at $V_{tip} = -1.15$ V and I_{tip}=20 nA. Each profile has been renormalized to have the same amplitude over the wide GaAs region. (f) Zoom-in view of the 15 nm wide QW. Reprinted with permission from Ref. [126]. (For interpretation of the references to colour in this figure legend, the reader is referred to the web version of this article.) © 2005, American Institute of Physics.
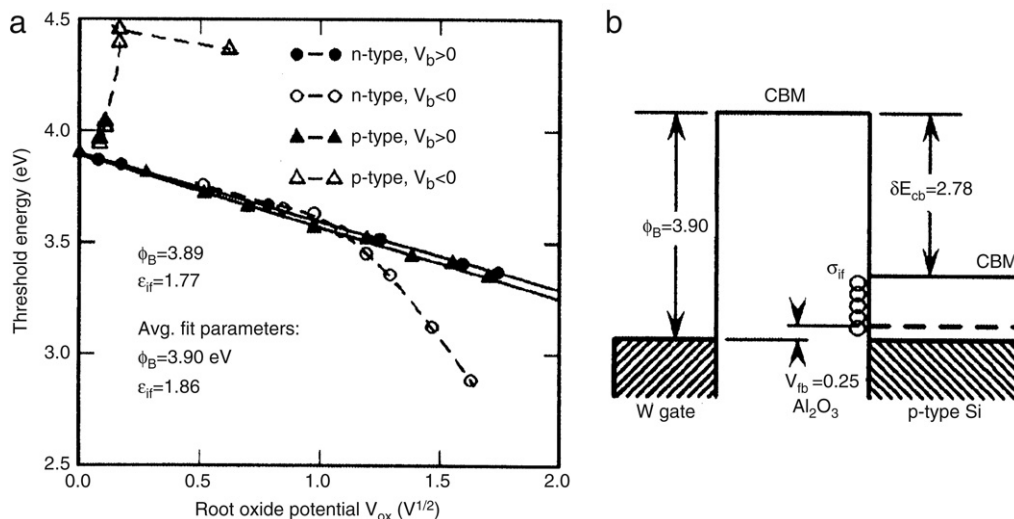

Fig. 28. (a) BEEM thresholds vs the square root of the oxide potential for a W/Al$_2$O$_3$/Si(100) MOS structure. (b) Energy band diagram in a flat-band condition with a p-type substrate. The circles represent unfilled trap levels of density σ_{if} near the oxide-Si substrate for $V_{ox} > 0$. Reprinted with permission from Ref. [86]. © 2002, Elsevier.

is obtained by solving the Poisson equation for the appropriate Si and oxide parameters. A linear dependency of V_{th} on the square root of oxide potential was found for both n- and p-type substrates at $V_b > 0$ (see Fig. 28). The Al$_2$O$_3$ barrier height of $\phi_S = 3.90 \pm$

0.03 eV was determined by the averaged zero-field intercept. An averaged image force dielectric constant of $\epsilon_{if} = 1.86 \pm 0.1$ was determined by the slope of the linear fit for all data sets, which is drastically lower than the static dielectric constant $\epsilon_0 \approx 8$–9.
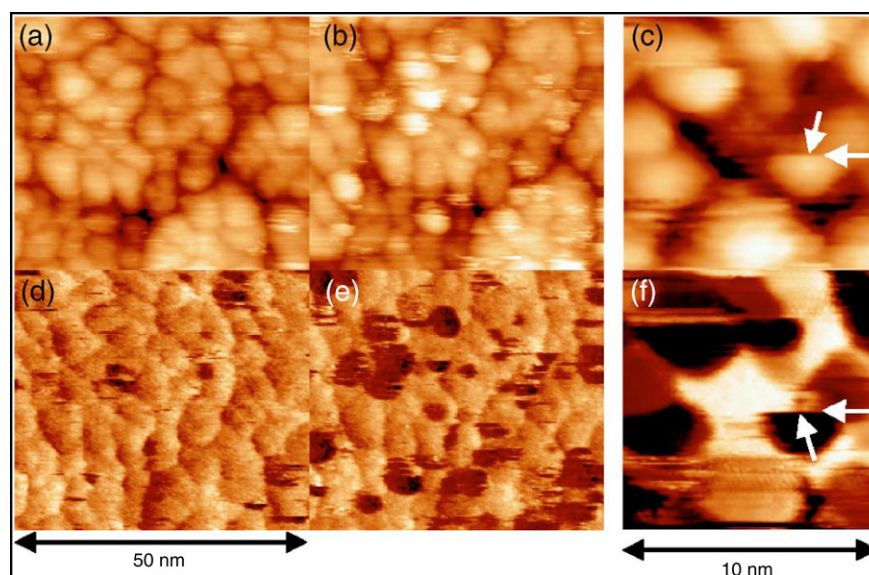
Fig. 29. Simultaneous STM (top) and BEEM (bottom) images on a Al(1 nm)/Co(1.2 nm)/Cu(1.2 nm)/Au(12 nm)/Si(111) sample exposed to a 10 Torr s high purity oxygen dose. (b) and (e) are scanned later than (a) and (d). The dark regions in BEEM images are clusters of chemisorbed O_2^-. (c) and (f) show images for a sample after annealed for 3 min at 375 °C. The abrupt vertical changes (arrows) are due to the movement of O_2^- caused by the tip scan. Reprinted with permission from Ref. [134].
© 2005, American Institute of Physics.

HfO_2 is one of the most promising dielectric materials to replace SiO_2 due to its high dielectric constant (~25) and a bandgap of 5.8 eV. Zheng et al. investigated a Au/HfO_2(4 nm)/SiO_2(1.5 nm)/Si structure using BEEM [132]. The HfO_2 films were grown by metal–organic chemical vapor deposition (MOCVD) on p-type Si(100) substrates (doping level ~10^{15} cm^{-3}). At a tip tunnel current of 1 nA and tip bias swept from 0 V to −5 V, the measured Schottky barrier height was ~3.8 eV and attributed to the interfacial SiO_2 layer. A HfO_2 barrier height of 1.9 eV was obtained after a local soft breakdown of the SiO_2 layer by sweeping the tip bias from −6 V to −1 V under a high injection current (≥5 nA). Oscillations in the BEEM current above the threshold voltage were observed. These oscillations were interpreted using Ludeke's model for quantum-size effects in the oxide conduction band. It should be noted that the existence of the SiO_2 interfacial layer unavoidably complicates the data interpretation making it preferable to study a clean HfO_2/Si interface.

Another approach is to utilize the oxide film as the topmost overlayer of the base films in the BEEM structure. Using this sample configuration, Perrella et al. studied amorphous AlO_x films (0.5–2.0 nm thick) grown on Co/Cu/Au/Si(111) [133]. STM topographical images revealed localized features on the exposed oxide surface which could not be uniquely identified as electronic defects or surface adsorbates (e.g. Fig. 29). By noting the change in the electron transport properties of these features in the accompanying BEEM images, it was determined that these localized features are chemisorbed O_2^-.

Similar work by Mather et al. investigated the as-grown and chemisorbed-oxygen covered surface of amorphous AlO_x thin films of ~1 nm thickness [134]. The chemisorbed oxygen ions were driven into the oxide by either electron bombardment or thermal annealing. A systematic change of the electronic states in the oxide was found. Both treatments greatly reduced the low energy band tail states and narrowed the DOS distribution over the oxide area.

7. Conclusion

In this article, we reviewed briefly the recent progress in several aspects of BEEM experiment and theory in the past few years. Orig-

inally invented as a unique microscopic and spectroscopic tool to probe metal–semiconductor interfaces, over the last two decades BEEM has been developed into a versatile method to exploit a wide range of metal, insulator and semiconductor materials and their interfaces. Excellent spatial resolution and independent control of the hot-carrier kinetic energies make this technique a powerful tool for nanometer-scale characterization of the structural and electronic properties of various nanostructures. Emphasis is given to those nanostructures that we consider are of great technological potential for next-generation electronic, spintronic and optoelectronic devices. These include ferromagnetic thin films and multilayers, organic thin films and molecules, and electroluminescence in semiconductor quantum dots, cross-sectional semiconductor heterostructures, and advanced insulator films. Many of these emerging fields are far from reaching a mature status, and therefore call for future BEEM studies to be done in the coming years.

References

[1] G. Binnig, H. Rohrer, C. Gerber, E. Weibel, Phys. Rev. Lett. 49 (1982) 57.
[2] G. Binnig, H. Rohrer, C. Gerber, E. Weibel, Phys. Rev. Lett. 50 (1983) 120.
[3] L.D. Bell, W.J. Kaiser, Phys. Rev. Lett. 61 (1988) 2368.
[4] W.J. Kaiser, L.D. Bell, Phys. Rev. Lett. 60 (1988) 1406.
[5] M. Prietsch, Phys. Rep. 253 (1995) 163.
[6] V. Narayanamurti, M. Kozhevnikov, Phys. Rep. 349 (2001) 447.
[7] J. Smoliner, D. Rakoczy, M. Kast, Rep. Prog. Phys. 67 (2004) 1863.
[8] V.P. LaBella, Y. Shusterman, L.J. Schowalter, C.A. Ventrice Jr., J. Vac. Sci. Technol. A 16 (1998) 1692.
[9] V.P. LaBella, C.A. Ventrice Jr., L.J. Schowalter, Appl. Surf. Sci. 123–124 (1998) 213.
[10] W.J. Kaiser, M.H. Hecht, L.D. Bell, F.J. Grunthaner, J.K. Liu, L.C. Davis, Phys. Rev. B 48 (1993) 18324.
[11] M.T. Cuberes, A. Bauer, H.J. Wen, M. Prietsch, G. Kaindl, Appl. Phys. Lett. 64 (1994) 2300.
[12] L.D. Bell, W.J. Kaiser, Annu. Rev. Mater. Sci. 26 (1996) 189.
[13] D.L. Smith, S.M. Kogan, Phys. Rev. B 54 (1996) 10354.
[14] J.J. O'Shea, E.G. Brazel, M.E. Rubin, S. Bhargava, M.A. Chin, V. Narayanamurti, Phys. Rev. B 56 (1997) 2026.

[15] D.L. Smith, E.Y. Lee, V. Narayanamurti, Phys. Rev. Lett. 80 (1998) 2433.
[16] M. Kozhevnikov, V. Narayanamurti, C. Zheng, Y.-J. Chiu, D.L. Smith, Phys. Rev. Lett. 82 (1999) 3677.
[17] D. Vashaee, A. Shakouri, Phys. Rev. Lett 92 (2004) 106103.
[18] K.J. Russell, I. Appelbaum, V. Narayanamurti, M.P. Hanson, A.C. Gossard, Phys. Rev. B 71 (2005) 121311.
[19] H. Sirringhaus, E.Y. Lee, H. von Kanel, Phys. Rev. Lett. 74 (1995) 3999.
[20] D.D. Awschalom, M.E. Flatté, N. Samarth, Sci. Am. 286 (2002) 52.
[21] D.D. Awschalom, J.M. Kikkawa, Phys. Today 52 (1999) 33.
[22] S. Datta, B. Das, Appl. Phys. Lett. 56 (1990) 665.
[23] M.N. Baibich, J.M. Broto, A. Fert, F. Nguyen Van Dau, F. Petroff, P. Etienne, G. Creuzet, A. Friederich, J. Chazelas, Phys. Rev. Lett. 61 (1988) 2472.
[24] G. Binasch, P. Grünberg, F. Saurenbach, W. Zinn, Phys. Rev. B 39 (1989) 4828.
[25] N.F. Mott, Philos. Trans. R. Soc. Lond. Ser. A 153 (1936) 699.
[26] J.S. Moodera, L.R. Kinder, T.M. Wong, R. Meservey, Phys. Rev. Lett. 74 (1995) 3273.
[27] M. Julliere, Phys. Lett. 54A (1975) 225.
[28] T. Miyazaki, N. Tezuka, J. Magn. Magn. Mater. 139 (1995) L231.
[29] I. Žutić, J. Fabian, S. Das Sarma, Rev. Mod. Phys. 76 (2004) 323.
[30] J. Fabian, A. Matos-Abiague, C. Ertler, P. Stano, I. Žutić, Acta Phys. Slovaca 57 (2007) 565.
[31] S.A. Wolf, D.D. Awschalom, R.A. Buhrman, J.M. Daughton, S. von Molnár, M.L. Roukes, A.Y. Chtchelkanova, D.M. Treger, Science 294 (2001) 1488.
[32] R.P. Lu, B.A. Morgan, K.L. Kavanagh, C.J. Powell, P.J. Chen, F.G. Serpa, W.F. Egelhoff Jr., J. Appl. Phys. 87 (2000) 5164.
[33] A.J. Stollenwerk, M.R. Krause, D.H. Idell, R. Moore, V.P. LaBella, Phys. Rev. B 74 (2006) 155328.
[34] A.J. Stollenwerk, M.R. Krause, D.H. Idell, R. Moore, V.P. LaBella, J. Vac. Sci. Technol. B 24 (2006) 2009.
[35] R.P. Lu, B.A. Morgan, K.L. Kavanagh, C.J. Powell, P.J. Chen, F.G. Serpa, W.F. Egelhoff Jr., J. Vac. Sci. Technol. B 18 (2000) 2047.
[36] A.J. Stollenwerk, M.R. Krause, R. Moore, V.P. LaBella, J. Vac. Sci. Technol. A 24 (2006) 1610.
[37] N.W. Ashcroft, N.D. Mermin, Solid State Physics, Saunders College, 1976.
[38] M.D. Stiles, D.R. Hamann, Phys. Rev. Lett. 66 (1991) 3179.
[39] M.D. Stiles, D.R. Hamann, Phys. Rev. B 38 (1988) 2021.
[40] H.D. Hallen, A. Fernandez, T. Huang, J. Silcox, R.A. Buhrman, Phys. Rev. B 46 (1992) 7256.
[41] M. Freyss, N. Papanikolaou, V. Bellini, R. Zeller, P.H. Dederichs, Phys. Rev. B 66 (2002) 014445.
[42] L.F. Mattheiss, D.R. Hamann, Phys. Rev. B 47 (1993) 13114.
[43] W.H. Rippard, R.A. Buhrman, Appl. Phys. Lett. 75 (1999) 1001.
[44] W.H. Rippard, R.A. Buhrman, J. Appl. Phys. 87 (2000) 6490.
[45] R. Heer, J. Smoliner, J. Bornemeier, H. Brückl, Appl. Phys. Lett. 85 (2004) 4388.
[46] E. Haq, H. Gokcan, T. Banerjee, F.M. Postma, M.H. Siekman, R. Jansen, J.C. Lodder, J. Appl. Phys. 95 (2004) 6930.
[47] W.H. Rippard, R.A. Buhrman, Phys. Rev. Lett. 84 (2000) 971.
[48] A.C. Perrella, P.G. Mather, R.A. Buhrman, J. Appl. Phys. 98 (2005) 093713.
[49] R. Wiesendanger, H.J. Guntherodt, G. Guntherodt, R.J. Gambino, R. Ruf, Phys. Rev. Lett. 65 (1990) 247.
[50] A.J. Stollenwerk, M.R. Krause, J.J. Garramone, E.J. Spadafora, V.P. LaBella, Phys. Rev. B 76 (2007) 195311.
[51] K. Mizushima, T. Kinno, T. Yamauchi, K. Tanaka, IEEE Trans. Magn. 33 (1997) 3500.
[52] K. Mizushima, T. Kinno, K. Tanaka, T. Yamauchi, Phys. Rev. B 58 (1998) 4660.
[53] S. van Dijken, X. Jiang, S.S.P. Parkin, Phys. Rev. B 66 (2002) 094417.
[54] S. van Dijken, X. Jiang, S.S.P. Parkin, Phys. Rev. Lett. 90 (2003) 197203.
[55] X. Jiang, S. van Dijken, R. Wang, S.S.P. Parkin, Phys. Rev. B 69 (2004) 014413.
[56] D.K. Guthrie, L.E. Harrell, G.N. Henderson, P.N. First, T.K. Gaylord, E.N. Glytsis, R.E. Leibenguth, Phys. Rev. B 54 (1996) 16972.
[57] D.L. Smith, M. Kozhevnikov, E.Y. Lee, V. Narayanamurti, Phys. Rev. B 61 (2000) 13914.
[58] S. van Dijken, X. Jiang, S.S.P. Parkin, Appl. Phys. Lett. 80 (2002) 3364.
[59] S. van Dijken, X. Jiang, S.S.P. Parkin, Appl. Phys. Lett. 83 (2003) 951.
[60] B.G. Park, T. Banjeree, B.C. Min, J.G.M. Sanderink, J.C. Lodder, R. Jansen, J. Appl. Phys. 98 (2005) 103701.
[61] J.M. Kikkawa, D.D. Awschalom, Phys. Rev. Lett. 80 (1998) 4313.
[62] Y. Ohno, D.K. Young, B. Beschoten, F. Matsukura, H. Ohno, D.D. Awschalom, Nature 402 (1999) 790.
[63] I. Appelbaum, B. Huang, D.J. Monsma, Nature 447 (2007) 295.
[64] B. Haung, D.J. Monsma, I. Appelbaum, J. Appl. Phys. 102 (2007) 013901.
[65] B. Haung, D.J. Monsma, I. Appelbaum, Phys. Rev. Lett. 99 (2007) 177209.
[66] B. Haung, D.J. Monsma, I. Appelbaum, Appl. Phys. Lett. 91 (2007) 072501.
[67] B. Haung, L. Zhao, D.J. Monsma, I. Applebaum, Appl. Phys. Lett. 91 (2007) 052501.
[68] Y. Yafet, in: F. Seitz, D. Turnbull (Eds.), Solid State Physics, vol. 14, Academic, New York, 1963.
[69] T. Banerjee, E. Haq, M.H. Siekman, J.C. Lodder, R. Jansen, Phys. Rev. Lett. 94 (2005) 027204.
[70] B.G. Park, T. Banerjee, J.C. Lodder, R. Jansen, Phys. Rev. Lett. 97 (2006) 137205.
[71] E. Haq, T. Banerjee, M.H. Siekman, J.C. Lodder, R. Jansen, Appl. Phys. Lett. 86 (2005) 082502.
[72] L.D. Bell, M.H. Hecht, W.J. Kaiser, L.C. Davis, Phys. Rev. Lett. 64 (1990) 2679.
[73] E. Heindl, J. Vancea, C.H. Back, Phys. Rev. B 75 (2007) 073307.
[74] F. Wöhler, Ann. Phys. Chem. 37 (1828) 330.
[75] J.W. Weigl, Angew. Chem. 89 (1977) 386.
[76] P. Peumans, A. Yakimov, S.R. Forrest, J. Appl. Phys. 93 (2003) 3693.
[77] C. Sanchez, B. Lebeau, F. Chaput, J.-P. Boilot, Adv. Mater. 15 (2003) 1969.
[78] H. Tian, S.J. Yang, Chem. Soc. Rev. 33 (2004) 85.
[79] L.S. Hung, C.H. Chen, Mater. Sci. Eng. R Rep. 39 (2002) 143.
[80] H.E. Katz, Z. Bao, J. Phys. Chem. B 104 (2000) 671.
[81] G. de la Torre, P. Vázquez, F. Agulló-López, T. Torres, J. Mater. Chem. 8 (1998) 1671.
[82] M.A. Reed, Proc. IEEE 87 (1999) 652.
[83] C. Troadec, L. Kunardi, N. Chandrasekhar, Appl. Phys. Lett. 86 (2005) 072101.
[84] P. Puschnig, C. Ambrosch-Draxl, Phys. Rev. B 60 (1999) 7891.
[85] B. Kaczer, H.-J. Im, J.P. Pelz, J. Vac. Sci. Technol. B 16 (1998) 2302.
[86] R. Ludeke, J. Non-Cryst. Solids 303 (2002) 150.
[87] F. Nüesch, F. Rotzinger, L. Si-Ahmed, L. Zuppiroli, Chem. Phys. Lett. 288 (1998) 861.
[88] H. Haick, M. Ambrico, T. Ligonzo, D. Cahen, Adv. Mater. 16 (2004) 2145.
[89] W. Li, K.L. Kavanagh, C.M. Matzke, A.A. Talin, F. Léonard, S. Faleev, J.W.P. Hsu, J. Phys. Chem. B 109 (2005) 6252.
[90] H. Haick, J.P. Pelz, T. Ligonzo, M. Ambrico, D. Cahen, W. Cai, C. Marginean, C. Tivarus, R.T. Tung, Phys. Status Solidi A 203 (2006) 3438.
[91] E.R. Heller, J.P. Pelz, Appl. Phys. Lett. 82 (2003) 3919.
[92] R.T. Tung, Phys. Rev. B 45 (1992) 13509.
[93] S. Özcan, J. Smoliner, M. Andrews, G. Strasser, T. Dienel, R. Franke, T. Fritz, Appl. Phys. Lett. 90 (2007) 092107.
[94] G. Kirczenow, Phys. Rev. B 75 (2007) 045428.
[95] H. Sirringhaus, E.Y. Lee, H. von Känel, Phys. Rev. Lett. 73 (1994) 577.
[96] I.B. Altfeder, J.A. Golovchenko, V. Narayanamurti, Phys. Rev. Lett. 87 (2001) 056801.
[97] A. Bannani, C. Bobisch, R. Möller, Science 315 (2007) 1824.
[98] Y. Arakawa, H. Sakaki, Appl. Phys. Lett. 40 (1982) 939.
[99] J.-Y. Marzin, J.-M. Gérard, A. Izraël, D. Barrier, G. Bastard, Phys. Rev. Lett. 73 (1994) 716.
[100] G.W. Bryant, Appl. Phys. Lett. 72 (1998) 768.
[101] J.K. Gimzewski, B. Reihl, J.H. Coombs, R.R. Schlittler, Z. Phys. B 72 (1988) 497.
[102] D.L. Abraham, A. Veider, C. Schönenberger, H.P. Meier, D.J. Arent, S.F. Alvarado, Appl. Phys. Lett. 56 (1990) 1564.
[103] P. Renaud, S.F. Alvarado, Phys. Rev. B 44 (1991) 6340.
[104] R.W. Rendell, D.J. Scalapino, Phys. Rev. B 24 (1981) 3276.
[105] F.J. Himpsel, Surf. Sci. Rep. 12 (1990) 3.
[106] C.L. Petersen, M.R. Frei, S.A. Lyon, Phys. Rev. Lett. 63 (1989) 2849.
[107] S.A. Lyon, C.L. Petersen, Semicond. Sci. Technol. 7 (1992) B21.
[108] I. Appelbaum, Ph.D. Thesis, Massachusetts Institute of Technology, Cambridge, MA 02139, 2003.
[109] K.J. Russell, I. Appelbaum, H. Temkin, C.H. Perry, V. Narayanamurti, M.P. Hanson, A.C. Gossard, Appl. Phys. Lett. 82 (2003) 2960.
[110] I. Appelbaum, K.J. Russell, V. Narayanamurti, D.J. Monsma, C.M. Marcus, M.P. Hanson, A.C. Gossard, H. Temkin, C.H. Perry, Appl. Phys. Lett. 82 (2003) 4498.
[111] I. Appelbaum, K.J. Russell, M. Kozhevnikov, V. Narayanamurti, M.P. Hanson, A.C. Gossard, Appl. Phys. Lett. 84 (2004) 547.
[112] W. Yi, I. Appelbaum, K.J. Russell, V. Narayanamurti, M.P. Hanson, A.C. Gossard, Appl. Phys. Lett. 85 (2004) 1990.
[113] W. Yi, Ph.D. Thesis, Harvard University, Cambridge, MA 02138, 2005.
[114] E.Y. Lee, S. Bhargava, M.A. Chin, V. Narayanamurti, J. Vac. Sci. Technol. A 15 (1997) 1351.
[115] E.Y. Lee, V. Narayanamurti, D.L. Smith, Phys. Rev. B 55 (1997) R16033.
[116] E.Y. Lee, Phys. Rev. B 59 (1999) 15332.
[117] D.W. Winston, Ph.D. Thesis, University of Colorado, Boulder, CO 80309, 1996.
[118] I. Appelbaum, W. Yi, K.J. Russell, V. Narayanamurti, M.P. Hanson, A.C. Gossard, Appl. Phys. Lett. 86 (2005) 063110.
[119] W. Yi, I. Appelbaum, K.J. Russell, V. Narayanamurti, R. Schalek, M.P. Hanson, A.C. Gossard, J. Appl. Phys. 100 (2006) 013105.
[120] W. Yi, V. Narayanamurti, J.M.O. Zide, S.R. Bank, A.C. Gossard, Phys. Rev. B 75 (2007) 115333.
[121] R.M. Feenstra, Semicond. Sci. Technol. 9 (1994) 2157.
[122] M.B. Johnson, J.-M. Halbout, J. Vac. Sci. Technol. B 10 (1992) 508.
[123] E.T. Yu, M.B. Johnson, J.-M. Halbout, Appl. Phys. Lett. 61 (1992) 201.
[124] E.T. Yu, J.-M. Halbout, A.R. Powell, S.S. Iyer, Appl. Phys. Lett. 61 (1992) 3166.
[125] C. Tivarus, J.P. Pelz, M.K. Hudait, S.A. Ringel, Phys. Rev. Lett. 94 (2005) 206803.
[126] C. Tivarus, J.P. Pelz, M.K. Hudait, S.A. Ringel, Appl. Phys. Lett. 87 (2005) 182105.
[127] D. Rakoczy, G. Strasser, J. Smoliner, Appl. Phys. Lett. 86 (2005) 202112.
[128] A.A. Talin, D.A.A. Ohlberg, R.S. Williams, P. Sullivan, I. Koutselas, B. Williams, K.L. Kavanagh, Appl. Phys. Lett. 62 (1993) 2965.
[129] S.M. Sze, Physics of Semiconductor Devices, John Wiley & Sons, New York, 1981.
[130] D. Landheer, Y. Tao, D.-X. Xu, G.I. Sproule, D.A. Buchanan, J. Appl. Phys. 78 (1995) 1818.
[131] E. Cartier, J.C. Tsang, M.V. Fischetti, D.A. Buchanan, Microelectron. Eng. 36 (1997) 103.
[132] Y. Zheng, A.T.S. Wee, K.L. Pey, C. Troadec, S.J. O'Shea, N. Chandrasekhar, Appl. Phys. Lett. 90 (2007) 142915.
[133] A.C. Perrella, W.H. Rippard, P.G. Mather, M.J. Plisch, R.A. Buhrman, Phys. Rev. B 65 (2002) 201403(R).
[134] P.G. Mather, A.C. Perrella, E. Tan, J.C. Read, R.A. Buhrman, Appl. Phys. Lett. 86 (2005) 242504.